ORNL/TM-2019/1025
Revision 0

Two-modulator Generalized Ellipsometry Microscope (2-MGEM) Examination of Concrete Aggregates

MILESTONE M3LW-19OR0403047, WORK PACKAGE: LW-19OR040304: IRRADIATED CONCRETE

June 2019

U.S. Department of Energy

Office of Nuclear Energy

ORNL/TM-2019/1025
Revision 0

Milestone M3LW-19OR0403047, Work Package: LW-19OR040304: Irradiated Concrete

TWO-MODULATOR GENERALIZED ELLIPSOMETRY MICROSCOPE (2-MGEM) EXAMINATION OF CONCRETE AGGREGATES

G. E. Jellison,[*] Jr., L. M. Anovitz[^] and T. M. Rosseel[*]
[*]Materials Science and Technology Division
[^]Chemistry Division

June 2019

Prepared by
OAK RIDGE NATIONAL LABORATORY
Oak Ridge, TN 37831-6283
managed by
UT-BATTELLE, LLC
for the

U.S. Department of Energy
Office of Nuclear Energy

CONTENTS

FIGURES

TABLES

ACRONYMS

EBSD	Electron beam backscatter diffraction
2-MGEM	two-modulator generalized ellipsometry microscope
N	Diattenuation = $(R_{max} - R_{min})/ (R_{max} + R_{min})$
γ	Principal axis direction. Polarized light direction of R_{max}.
US	Universal stage
CIP	computer-integrated polarization microscopy
PEM	Photoelastic Modulator
mXRF	micro x-ray fluorescence
PSG	Polarization state generator
PSA	Polarization state analyzer

EXECUTIVE SUMMARY

The examination of the microstructure of geological materials (and therefore aggregates found in concrete) is a complicated endeavor. The crystals found in natural rocks can vary is size from submicron to centimeters. Moreover, these crystals can have different chemical composition and orientation. To complicate things more, crystals of the same chemical composition can have different crystal structure [Example: $CaCO_3$ can be calcite (trigonal), aragonite (orthorhombic) or vaterite (hexagonal); Carbon can be diamond (cubic) or graphite (hexagonal), etc.] Geologists continue to struggle with examination techniques to quantify the structure of rocks. Since the aggregates used in concrete are just rocks, the study of concrete has similar concerns.

The two-modulator generalized ellipsometry microscope (2-MGEM) has been used for the last ~10 years for the characterization of the IPyC (inner pyrolytic carbon) layer in TRISO (tristructural-isotropic) nuclear fuel. The instrument works at near-normal incidence reflection and measures the optical diattenuation N [= $(R_{max} - R_{min})/(R_{max} + R_{min})$, where R_{max} (R_{min}) is the polarization-dependent maximum (minimum) reflectivity] and the principal angle γ, which is the angle of the polarization direction of the maximum reflectivity. The accuracy of the N measurement is ±0.001 out of 1, while the accuracy of γ can be as good as 0.2°, depending on the value of N. If the sample is isotropic then the diattenuation N is near 0 and the principal axis γ is indeterminate. The present 2-MGEM has an optical resolution of ~6 microns.

Interest in this technique has grown since it provides a simple characterization technique for aggregates in concrete which can degrade over time, particularly in nuclear reactors. Interest in the effects of radiation on minerals, aggregates, and concrete, which began in the 1950s to better understand radiation shielding properties, has seen a recent resurgence based, in no small measure, upon a renewed focus on the management of aging national nuclear fleets and lifetime extension considerations to meet future national energy needs (Rosseel et al., 2016).

In this report, 2-MGEM analyses of minerals and rocks commonly found in aggregates and concrete are described. The 2-MGEM measurements may provide a needed tool to characterize mineral phases and the degree of crystallinity in concrete and offers a technique that is relatively simple and can be performed in air and on samples that are easy to prepare. When combined with X-ray Fluorescence (XRF) mapping using Microstructure-Oriented Scientific Analysis of Irradiated Concrete (MOSAIC) (Giorla, 2018, Le Pape, et al, 2019a and 2019b), these methods could form the basis of a toolkit to determine the sensitivity of concrete specimen to neutron irradiation.

Calcite ($CaCO_3$) and dolomite ($CaMg(CO_3)_2$) are both common crystals found in limestone or marble and therefore common aggregate materials. Optically, they are both uniaxial with a large birefringence so are particularly easy to examine with the 2-MGEM. Since these materials are uniaxial, the measurement of N and γ is sufficient to determine the direction of the optic axis of a crystallite. The angle of the optic axis with respect to the sample surface is given by $\theta = \text{asin}((N/N_{max})^{0.5})$ where N_{max} is the maximum diattenuation as determined by the refractive indices ($N_{max} = 0.23$ for calcite and dolomite). The accuracy of θ depends on the magnitude of N and is more inaccurate when N/N_{max} is close to 0 or near 1. When the diattenuation is large, the accuracy of γ (or ϕ, the angle of the optic axis projection onto the sample surface with respect to the laboratory reference frame) can be as good as 0.2°. For these materials, it is possible to construct an optical pole figure from a sample, which maps the number of pixels where the optic axis points in the (θ, ϕ) direction.

Aragonite is a polymorph of calcite, having the same chemical formula but the orthorhombic crystal structure. The refractive index for light polarized along the c-axis n_c is significantly less than for light polarized along the a- or b-axes n_a and n_b, but n_b-n_a is small, making aragonite nearly uniaxial. If the c-axis is pointing significantly off the surface normal, then N and γ are accurately measured, from which it is possible to determine θ and ϕ quite accurately; the angle ψ (rotation about the c-axis) is indeterminant. If the c-axis is pointing near the surface normal, then N is small, and γ is measured inaccurately. The

small value of N can be due either to a small tilt of the c-axis with respect to the surface normal or to the small difference between n_a and n_b.

Silicate materials, such as quartz and fledspars, are primarily based on the SiO_4 unit. These units are isotropic with no birefringence if the unit is undistorted. Even α quartz (SiO_2) has distorted SiO_4 units making the crystal trigonal; quartz also has no inversion symmetry point, making it optically active. Virtually all feldspar silicate rocks have low symmetry (monoclinic or triclinic) and therefore some birefringence, but the birefringence is usually small. Nevertheless, 2-MGEM images do show differences in the N and γ coming from different crystallites; as such, the 2-MGEM does show grain boundaries.

The 2-MGEM results have also been compared with electron beam backscattering diffraction (EBSD), which is presently the standard technique for the characterization of crystallites in rocks. While EBSD measurements can be used to determine actual crystallographic orientation, they require a scanning electron microscope (SEM), must be performed in vacuum, require a thin graphite layer to avoid charging, examine only the top ~5 nm of the sample, and can be susceptible to image distortion for large area images. On the other hand, 2-MGEM measurements are performed in air, do not require any additional layer, and are not susceptible to image distortion. This work shows that the 2-MGEM technique is a useful technique to study the microstructure of rocks.

The data from the 2-MGEM is shown to be extremely useful in characterizing carbonate-based crystallites. If an aggregate in concrete has crystallites with high diattenuation (N~0.23), then it is clear that the crystallite is a carbonate. Moreover, the 2-MGEM images do indicate grain boundaries and, in many cases, can be used to determine the orientation of the optic axis. Because most silicate materials have significantly lower birefringence and are of lower symmetry, less can be determined from 2-MGEM measurements. However, the ability to determine grain boundaries in these rocks is of considerable value.

1. INTRODUCTION

The crystallographic orientation of crystallites is an important piece of information for structural geologists studying the formation of rocks and their subsequent evolution. The earliest technique commonly employed for crystallographic orientation of crystallites in rocks is based on the universal stage (US, Berek 1924). Later Panozzo-Heilbronner and Pauli (1993) introduced computer-integrated polarization microscopy (CIP), which significantly improved the time required for crystallite orientation determination. Both techniques are optical transmission measurements and require thin section sample preparation. Today, many geologists are using electron backscatter diffraction (EBSD) measurements for crystallographic orientation determination, which is a surface technique utilizing a scanning electron microscope. In this report, we describe the two-modulator generalized ellipsometry microscope (2-MGEM) as a new technique to characterize crystallites found in geological rocks and therefore aggregates in concrete.

This report will discuss the use of the 2-MGEM to characterize several mineral, rock, and concrete samples. The rock samples include carbonate minerals, such as calcite, dolomite and aragonite, feldspars, such as microcline, orthoclase, and labradorite, and granite, which is composed primarily of quartz and feldspars. The only requirements are that the sample be polished to nearly optical quality and that the sample be reasonably optically anisotropic with the optic axis not perpendicular to the sample surface. The 2-MGEM data can be used to determine the optic axis of uniaxial crystals such as calcite and dolomite. Orthorhombic samples such as aragonite (a polymorph of calcite) can also be examined using the 2-MGEM, and the direction of the c-axis determined if the c-axis is not near-normal to the sample surface. While the 2-MGEM cannot determine the optical axes of lower symmetry crystals, it can often be used to identify the positions of crystallites, including grain boundaries, within the optical resolution of the instrument. Since about 95% of known inorganic materials are anisotropic (Newnham, 2005), this technique may find widespread application in geology. Obvious applications include the measurement of strain fields in deformed rocks and the study of aggregates in concrete under various environmental conditions such as radiation fields.

The 2-MGEM results are also compared with electron backscatter diffraction (EBSD) measurements taken on some of the calcite, dolomite, and aragonite samples. EBSD is a technique that has been in use in the geological sciences for two decades (Prior et al., 1999; Prior et al., 2009), and can be used to determine the crystallographic orientation of crystallites in rock samples. The EBSD technique relies on the diffraction of electrons that hit a phosphor screen and are then detected using a digital camera. The resulting Kikuchi patterns are interpreted using a complicated mathematical algorithm to determine the crystal structure and local three-dimensional crystal orientation of each pixel, as expressed using Euler angles. The comparisons presented here will show that the 2-MGEM results compare favorably with electron backscatter diffraction (EBSD) measurements on the same samples.

Our primary interest in this technique is that it provides a simple characterization technique for aggregates in concrete which can degrade over time, particularly in nuclear reactors. Interest in the effects of radiation on minerals, aggregates, and concrete, which began in the 1950s to better understand radiation shielding properties, has seen a recent resurgence based, in no small measure, upon a renewed focus on the management of aging national nuclear fleets and lifetime extension considerations to meet future national energy needs (Rosseel et al., 2016). Moreover, expert panels in both the US and Japan reached similar conclusions: there is an urgent need to develop a consistent knowledge base to better understand, model, and predict the effects of irradiation on structural concrete in US nuclear power plants (NPPs) (Graves et al., 2014; JNESO, 2013). To address these issues, Oak Ridge National Laboratory (ORNL), through the support of the US DOE Light Water Reactor Sustainability (LWRS) Program has developed parallel efforts to evaluate the effects of radiation under controlled conditions on mineral analogues of concrete aggregates and to combine optical and X-ray microscopy mapping to identify crystal boundaries and orientations of minerals in reactor cavity concrete aggregates. These features are a

critical to understanding radiation-induced micro cracking. The 2-MGEM measurements could provide a needed tool to characterize mineral phases and the degree of crystallinity in concrete and offers a technique that is relatively simple and can be performed in air and on samples that are easy to prepare. When combined with X-ray Fluorescence (XRF) mapping using Microstructure-Oriented Scientific Analysis of Irradiated Concrete (MOSAIC) (Giorla, 2018, Le Pape, et al, 2019a and 2019b), these methods could form the basis of a toolkit to determine the sensitivity of concrete specimen to neutron irradiation.

Over the course of the work, we have examined approximately 45 samples, measuring 4-8 regions of each sample. The samples included both single crystals and polycrystalline materials, uniaxial materials (calcite and dolomite), orthorhombic materials (aragonite), monoclinic and triclinic feldspars, granite and several different samples of concrete. This report selectively describes these results in our attempt to quantify the usefulness of the 2-MGEM to study rocks.

2. DESCRIPTION OF THE INSTRUMENT

The two-modulator generalized ellipsometry microscope (2-MGEM) (Jellison and Modine, 1997; Jellison et. al 2006) is a generalized ellipsometer configured at near-normal incidence operating a 577 nm (see Figure 1). The instrument consists of two polarizer-photoelastic modulator (PEM) pairs operating at different frequencies. Source light first enters the PSG (0) which consists of a polarizer oriented at 45° with respect to the principal vibrational axis of a PEM oscillating at ~50 kHz. This generates a dynamically elliptically polarized light beam, which is then incident upon the sample. The light reflected from the sample is then directed to the polarization state analyzer (PSA, 1), which is just another PEM-polarizer pair, where the frequency of the PEM is ~60 kHz. The resultant light beam is then directed to a photomultiplier tube detector, which records the intensity at a single wavelength using an analog-to-digital converter digitizing at 2 MHz. This waveform is then Fourier analyzed to determine the relevant parameters. The intensity of this waveform is given by

$$\text{Intensity}(t) = I_{DC} + I_{X0}X_0 + I_{Y0}Y_0 + I_{X1}X_1 + I_{Y1}Y_1 + I_{X0X1}X_0X_1 + I_{X0Y1}X_0Y_1 + I_{Y0X1}Y_0X_1 + I_{Y0Y1}Y_0Y_1 \quad (1a)$$

where

$$X_i = \sin(A_i\sin(\omega_i t)); \; Y_i = \cos(A_i\sin(\omega_i t)), \; i = 0, 1. \quad (1b)$$

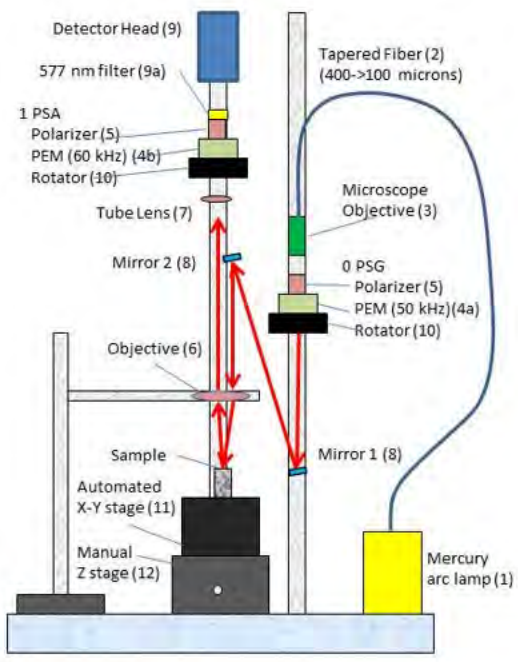

Figure 1. Schematic of the two-modulator generalized microscope (2-MGEM)

The quantities A_0, A_1 are the amplitudes of vibration of the PEMs and $2\pi\omega_0$, $2\pi\omega_1$ are the vibrational frequencies of the PEMs. The 8 parameters I_{X0}, I_{Y0}, etc. represent 8 elements of the sample Mueller matrix, where the selected elements are determined by the azimuthal orientation of the PSG and PSA. Since the frequencies of the PEMs are known very accurately, the digitized intensity vector of Eq. 1a can be Fourier analyzed to determine the 8 parameters I_{X0} I_{Y0}, etc. All 8 parameters are determined from the same waveform, so refer to the same experimental conditions. The measured parameters are normalized to I_{DC} and will be -1 to 1, with an accuracy of ~0.001.

The optical resolution of the instrument is presently ~6 microns. This is determined mostly by the focal length of the objective (6 in Figure 1), which is 10 cm. and the pinhole in front of the detector (25 microns). In some early experiments (Jellison and Hunn, 2008), the resolution was improved to ~3-4 microns by using an objective with a 5 cm. focal length. Reconfiguring the present 2-MGEM is not presently possible since the instrument is also used to qualify TRISO nuclear fuel for the Advanced Gas Reactor (AGR) program of DOE.

The image intensity is also recorded by the instrument. This is the equivalent to the image one would obtain with a large f-number microscope with f-number ~12. Light scattered or reflected out of the collection cone of the instrument does not contribute to the image, nor is it included in the determination of the data of the instrument.

At normal incidence, the definitions of measured parameters are different from those of standard ellipsometry (Jellison et. al 2006, Jellison et. al 2018). If the sample is isotropic or a uniaxial material with the optic axis perpendicular to the sample surface, then the sample does not change the polarization state resulting in the off-diagonal elements of the Mueller matrix becoming the zero. However, the sample Mueller matrix for a uniaxial material with the optic axis off the normal to the sample surface becomes

$$M = \begin{bmatrix} 1 & -C_{2\gamma}N & -S_{2\gamma}N & 0 \\ -C_{2\gamma}N & C_{2\gamma}^2 - S_{2\gamma}^2 C & C_{2\gamma}S_{2\gamma}(1+C) & S_{2\gamma}S \\ S_{2\gamma}N & -C_{2\gamma}S_{2\gamma}(1+C) & -S_{2\gamma}^2 + C_{2\gamma}^2 C & C_{2\gamma}S \\ 0 & S_{2\gamma}S & C_{2\gamma}S & C \end{bmatrix} \quad (2a)$$

In Equation 2a, $S_{2\gamma} = \sin(2\gamma)$ and $C_{2\gamma} = \cos(2\gamma)$, where γ is the angle of the projection of the principal axis with respect to the reference frame of the instrument. The quantities N, S, and C are given by

$$N = \frac{R_{max} - R_{min}}{R_{max} + R_{min}} \quad (2b)$$

$$S = \sqrt{1 - N^2}\sin(\delta) \quad (2c)$$

$$C = \sqrt{1 - N^2}\cos(\delta) \quad (2d)$$

$$\beta = 1 - \sqrt{N^2 + S^2 + C^2} \quad (2e)$$

where R_{max} and R_{min} are the maximum and minimum polarization-dependent reflectivities and δ is the retardation difference (i.e. $\delta = \delta_{max} - \delta_{min}$). The quantity β is a measure of depolarization and is 0 for a non-depolarizing sample.

The 2-MGEM measures 8 elements of the sample Mueller matrix, where the elements measured depend upon the azimuthal orientation of the PSG and the PSA. Normally, 2-MGEM measurements are taken in the (0°, 45°) configuration, where the measured elements are:

$$M_{measured} = \begin{bmatrix} 1 & \blacksquare & I_{Y0} & I_{X0} \\ I_{Y1} & \blacksquare & I_{Y0Y1} & I_{X0Y1} \\ \blacksquare & \blacksquare & \blacksquare & \blacksquare \\ I_{X1} & \blacksquare & I_{Y0X1} & I_{X0X1} \end{bmatrix} \quad (3)$$

The black squares indicate unmeasured Mueller matrix elements, which can be measured using different azimuthal orientations of the PSG and PSA. In this configuration, the depolarization factor β_{meas} is determined by 5 measured parameters:

$$\beta_{meas} = 1 - \sqrt{I_{Y0}^2 + I_{Y1}^2 + I_{X0Y1}^2 + I_{Y0X1}^2 + I_{X0X1}^2} \quad (4)$$

By comparing the elements of Eqs. 2a and 3, it can be seen that the 2-MGEM measures 4 quantities:

1. The diattenuation N. This quantity is 0 for reflection from an isotropic sample or for a uniaxial sample with the optic axis perpendicular to the sample surface.
2. Retardation difference $\delta = \delta_{max} - \delta_{min}$. For insulators with little or no overlayer (thin film or surface roughness), this is usually close to 0. This quantity can be significantly different from zero if the material is absorbing at the wavelength of the 2-MGEM, such as highly oriented pyrolytic graphite (Jellison et al. 2007).
3. The principal axis angle γ. The 2-MGEM measured parameters are the same if $\gamma \rightarrow \gamma + 90°$ and N, δ change signs. For uniaxial materials, the principal axis is parallel to the projection of the optic axis for positive birefringent materials and perpendicular to the projection of the optic axis for negative birefringent materials such as calcite and dolomite.

4. The depolarization fraction β. For most samples, β is close to 0. If β is significantly greater than 0, then the pixel being examined is depolarizing the light and the measurement cannot be trusted. For these measurements, depolarization may be due to voids in the sample surface, which would scatter the light, or from multiple crystallites in the measured pixel, which would scramble the measured polarization state, thereby reducing the reliability of the measurement for that pixel.

Another parameter measured with the 2-MGEM from the parameters I_{X0} and I_{X1} is the circular diattenuation CD = $(R_{rc} - R_{lc}) / (R_{rc} + R_{lc})$ where R_{rc} (R_{lc}) is the reflectivity for right-circularly (left circularly) polarized light. For samples with no chirality, this is close to 0.

For uniaxial crystals, it can be shown that the angle of the optic axis with respect to the sample surface is given by

$$N = N_{max} sin^2(\theta) \tag{5}$$

where the maximum diattenuation N_{max} is determined by the ordinary and extraordinary refractive indices n_o and n_e and the birefringence $\Delta n = n_o - n_e$.

$$|N_{max}| = \frac{2\varsigma}{1+\varsigma^2} \quad \varsigma = \frac{|\Delta n|}{n_o n_e - 1} \tag{6a, 6b}$$

3. RESULTS

3.1 Calcite and Dolomite (Jellison et. al 2018)

Both calcite ($CaCO_3$) and dolomite ($CaMg(CO_3)_2$) are commonly found in nature, often designated as limestone, and therefore are very important minerals for geologists and as aggregates in concrete. Both crystals have trigonal symmetry and are therefore optically uniaxial where the optic axis is aligned with the 3-fold rotational axis of the crystal. Calcite belongs to the point group $\bar{3}m$ (or D_{3d} Schönflies notation) and space group $R\bar{3}c$, and dolomite, with fewer symmetry operations, belongs to the point group $\bar{3}$ (or C_{3i} Schönflies notation) and space group $R\bar{3}$. The unit cells are large with a = 0.499 nm, c = 1.706 nm for calcite and a = 0.480 nm, c = 1.600 nm for dolomite. Because both calcite and dolomite consist of aligned CO_3 units (Bragg, 1924), the resulting birefringence is high. The large birefringence coupled with the high optical quality of calcite makes calcite a good starting material for the manufacture of optical devices, including polarizing prisms, beam displacers, depolarizers, etc. Consequently, the optical properties of calcite are considerably better known than they are for dolomite. The spectroscopic refractive indices of both calcite and dolomite have been measured and discussed in Jellison et. al (2018), from which the maximum diattenuation can be determined using Eq. 5. At 577 nm, $N_{max} = 0.2308 \pm 0.0019$ for both calcite and dolomite.

Figure 2 shows some representative data from a dolomite crystal purchased from Fabre Minerals, and came from the Asturreta Quarry in Navarre, Spain. The sample was cut such that the optic axis of the largest crystal (regions 1 and 6 of Figure 2) lay in the surface plane; this was confirmed by Laue x-ray scattering. The region of the mineral shown in Figure 2 shows many different crystallites where the optic axis points in many different directions. The 2-MGEM measured quantities are the diattenuation N and the direction of the principal axis γ. The depolarization β, retardation difference δ and the circular diattenuation CD are all near 0 over all the region examined, indicating a good measurement for an insulating sample. While the optical image shows many of the crystallites, it does not show all of them, and gives no indication of the orientation of the optic axis of the crystallites. The 2-MGEM data does give a good indication of the crystallites and their boundaries, within the optical resolution of the instrument.

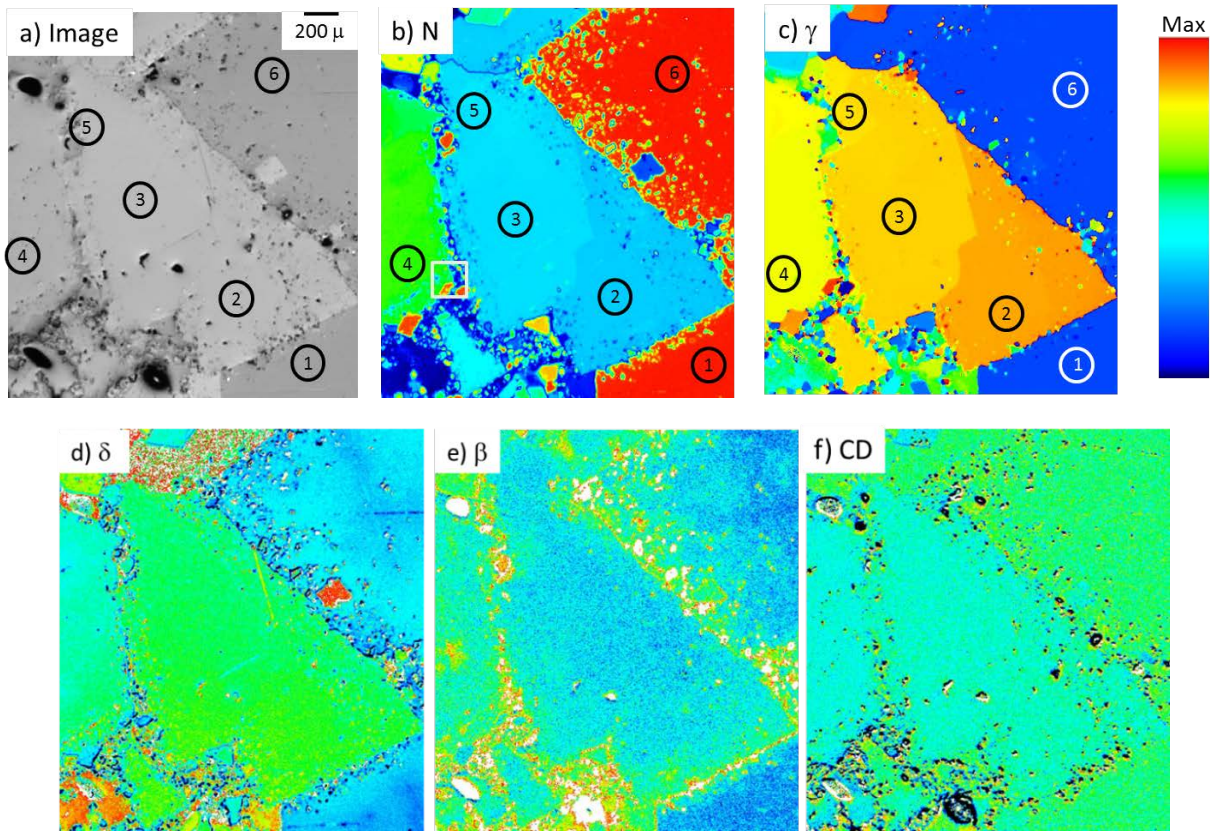

Figure 2. 2-MGEM data from a crystal of dolomite. The a) image, b) diattenuation N (Min – Max = 0 – 0.23), c) direction of the principal axis γ (-90° - 90°), d) Retardation δ (-0.031 - 0.008), e) Depolarization β (-0.005 – 0.005) and f) Circular diattenuation CD (-0.005 – 0.005) for a portion of a dolomite crystal. The size of the region examined is 2.030 x 2.235 mm (407 x 448 = 182336 pixels). The circled numbers indicate regions described in the text. The values are on a color scale shown above to the right with the maxima and minima for each quantity shown above. White is above the maximum and black is below the minimum.

Table 1 gives the values of the diattenuation, principal axis angle, and the calculated angle of the optic axis with respect to the surface normal θ from Eq. 5 of the numbered regions in Figure 2. EBSD measurements were also performed on several of the numbered regions and agree with the 2-MGEM results (Jellison et. al 2018; see the Appendix 6.1). An optical pole figure histogram of the data shown in Fig. 2 can be constructed, as shown in Fig. 3. This pole figure represents a 2-dimensional histogram where γ is divided into 180 equal segments, and θ is divided into 45 segments, but the incremental size is proportional to θ sin(θ). Thus, each 2-dimensional segment corresponds to an equal area on the unit sphere. The center of the semicircle corresponds to θ = 0, where the optic axis is along the surface normal, and the outer edge of the semicircle corresponds to the optic axis lying parallel to the sample surface. The direction of the fast axis is perpendicular to the optic axis and is dependent on the orientation of the sample in the instrument. It is restricted to a range of 180° (recall that the 2-MGEM cannot distinguish between (γ, N) and (γ + 90°, -N)). For the case of the data presented in Fig. 3, the range of γ is -90° at the left of the figure to +90° and the right of the figure.

Table I. The average values and standard deviations of the diattenuation and direction of the principal axis γ determined from the regions selected in Fig. 2. The angle θ of the optic axis off the surface normal is calculated from the diattenuation using Eq. 5. The standard deviations are quoted as ±1σ (Jellison, et. al 2018)

Region	N	θ (°)	γ (°)
1	0.2261±0.0019	82.0±3.3	-63.7±0.2
2	0.0764±0.0010	35.1±0.4	66.2±0.6
3	0.0823±0.0011	36.7±0.4	60.2±0.6
4	0.1397±0.0011	51.1±0.6	50.4±0.3
5	0.0830±0.0014	36.9±0.5	58.5±0.5
6	0.2261±0.0019	82.0±3.3	-63.7±0.3

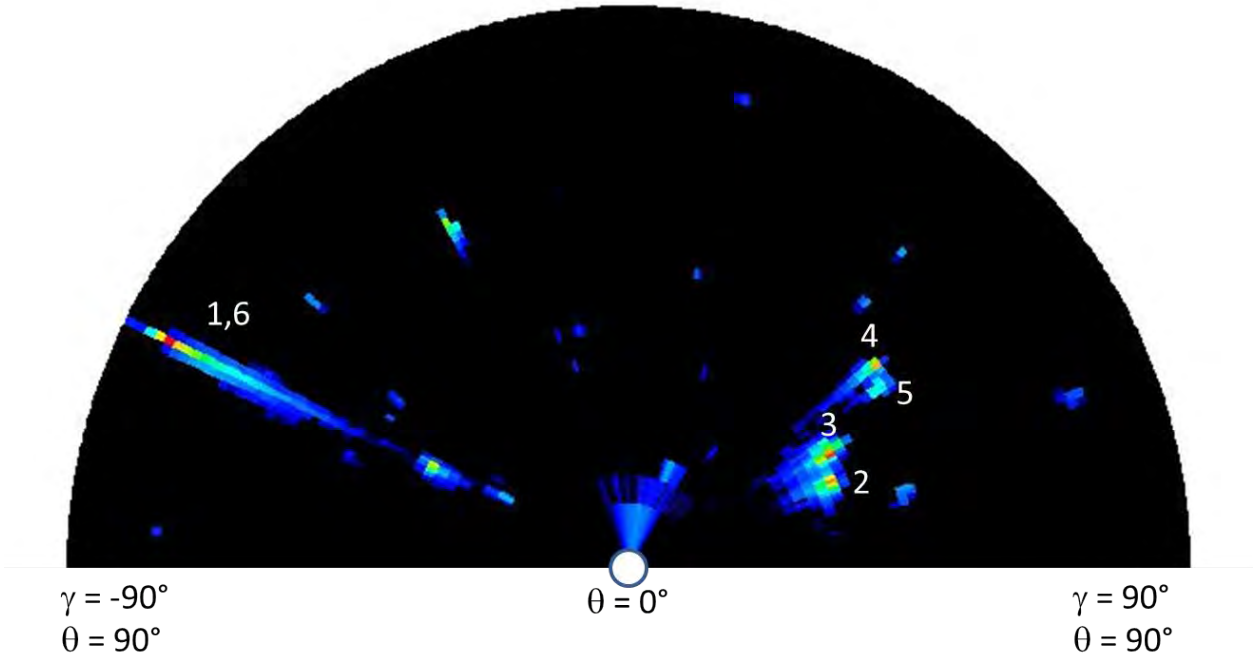

Figure 3. 2-dimensional optical pole figure histogram of the direction of the optic axis with respect to the surface normal. The angle θ is the angle of the optic axis with respect to the surface normal and the angle γ is the principal axis angle, perpendicular to the optic axis. The value (θ = 0°) is denoted by the circle, where θ increases with the radius and γ increases clockwise from -90° to +90°. There are 180 evenly divided γ segments and 45 θ sin(θ) segments such that each 2-dimensional segment corresponds to an equal area on the unit sphere. The numbers refer to the regions shown in Fig. 2 (Jellison, et. al 2018).

Similar measurements have also been performed on a Carthage Marble from Carthage, Missouri, USA. This material is a limestone and a chemical analysis shows that it is nearly all $CaCO_3$ (98.6%), with

a small amount of $MgCO_3$ (~0.6%) and trace amounts of iron oxides and alumina. A typical data set is shown in Figure 4, along with electron backscatter diffraction (EBSD) data.

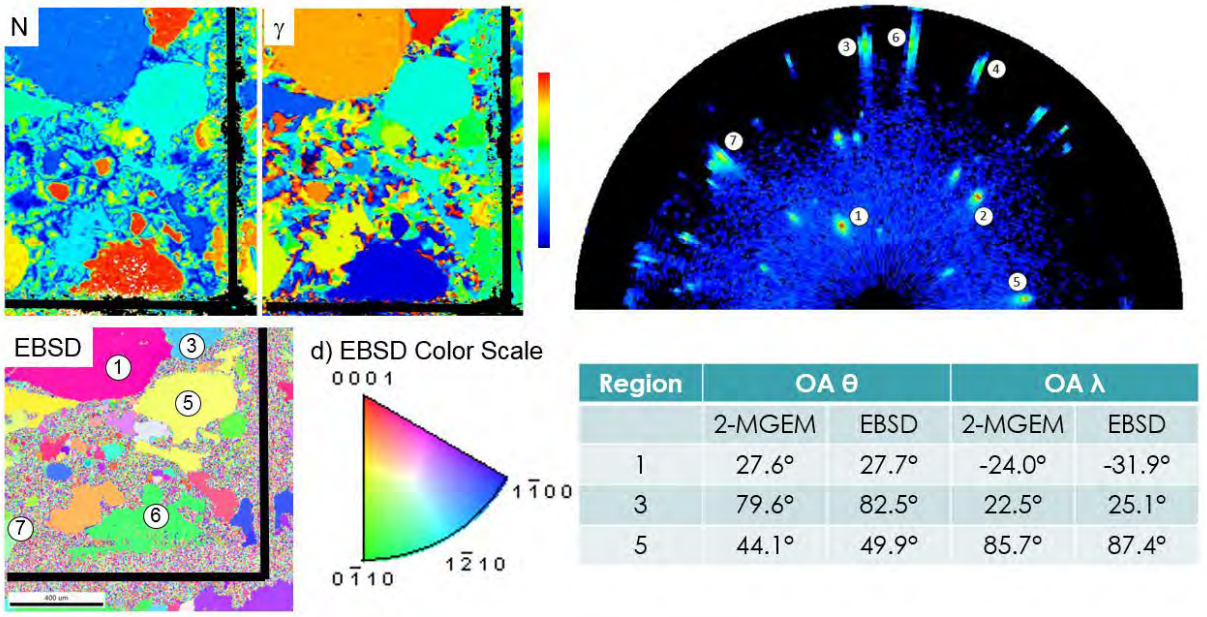

Region	OA θ		OA λ	
	2-MGEM	EBSD	2-MGEM	EBSD
1	27.6°	27.7°	-24.0°	-31.9°
3	79.6°	82.5°	22.5°	25.1°
5	44.1°	49.9°	85.7°	87.4°

Figure 4. Comparison of the 2-MGEM data with EBSD data for the Carthage Marble sample. a) 2-MGEM diattenuation N; b) 2-MGEM principal axis angle γ; c) EBSD data presented as the inverse pole figure with 0001 projected out of the page and d) the color scale for the EBSD data. The 2-MGEM data was taken on a 5 x 5 μ grid, while the EBSD data was taken on a 10 x 10 μ grid. The optical pole figure from the 2-MGEM data is shown in the upper right, and comparisons of the 2-MGEM and EBSD data at selected regions of the crystal is shown in table to the lower right. (Jellison et. al 2018)

As can be seen, there is general agreement between the 2-MGEM data and the EBSD data. The speckled regions of the EBSD data represent regions where the computer algorithm of the SEM could not determine the crystallographic orientation of the crystallite.

3.2 Aragonite (Jellison et. al 2019)

Aragonite is another common geological material that has the same chemical composition as calcite ($CaCO_3$), but with a different crystal structure. While calcite is uniaxial with only two different refractive indices at each wavelength, aragonite is orthorhombic with three different refractive indices at each wavelength. Aragonite is named for the Molina de Aragón region in Castilla-La Mancha, Spain, and is found in many other places around the globe. It can be formed either geologically under high temperature and pressure or biologically, as it is found naturally in the shells of many mollusks. Under the temperature and pressure conditions at the earth's surface, aragonite will transform to calcite in 10^4 to 10^8 years (Davis and Adams, 1965; Huang, 2003). Because of its relationship to calcite, aragonite is an important geological material. As discussed above, $CaCO_3$ is one of several primary constituents of concrete aggregates, which can degrade in nuclear environments due to neutron-induced swelling and subsequent cracking. Efforts to evaluate these radiation effects under controlled conditions on mineral analogues of concrete aggregates (Rosseel et al, 2017 and Silva et al, 2018) and to combine optical and X-ray microscopy mapping of minerals in concrete aggregates to identify crystal boundaries and orientations are underway (Le Pape et al., 2019) and are a critical to understanding radiation-induced micro cracking reactor cavity concrete.

The samples of this study were taken from a natural aragonite sample obtained from the aragonite mine from the Molina de Aragon region in Castilla-La Mancha, Spain. Four samples were cut: 3 such that the c-axis (with the lowest refractive index) lying nearly parallel to the sample surface, and the fourth with the c-axis nearly perpendicular to the sample surface. As with the calcite and dolomite samples discussed above, Laue x-ray and EBSD measurements were also made on these samples to give an indepentent verification of the results obtained from the 2-MGEM measurements.

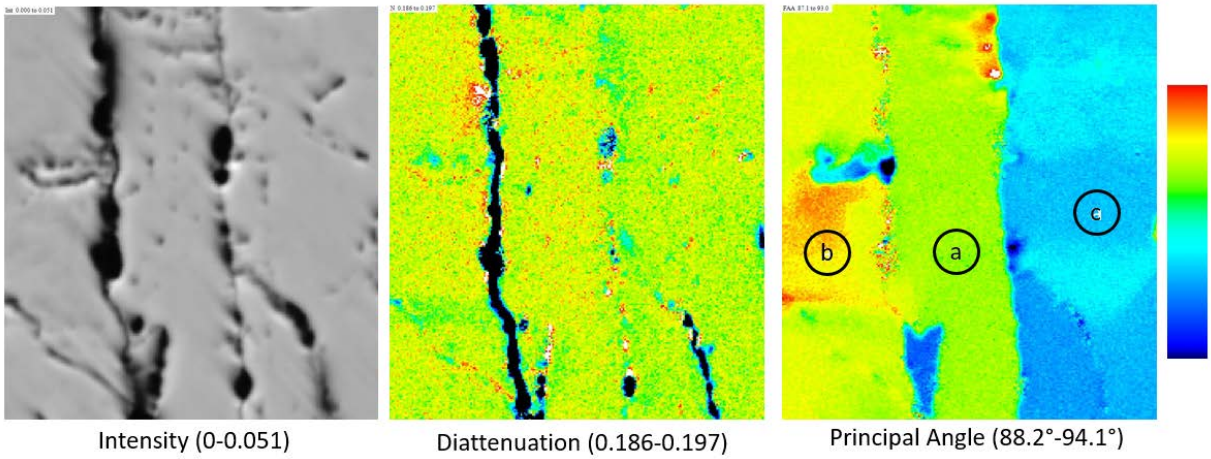

Figure 5. 2-MGEM data from a sample cut with the c-axis nearly parallel to the sample surface. The color scale is to the right and the values in parentheses give the ranges. The scale is 1.12 X 1.24 mm.

Table II. Values of the diattenuation N and direction of the principal axis γ for the regions indicated in Figure 5.

Region	N	γ
a	0.1936±0.0011	92.0°±0.2°
b	0.1938±0.0008	92.8°±0.3°
c	0.1934±0.0008	90.1°±0.2°

Figure 5 shows 2-MGEM images of a region containing grain boundaries from a sample that is cut such that the c-axis lies nearly in the surface plane of the sample. Three sub-regions were selected for further analysis, as indicated by the circled letters in Figure 5, and the resulting data are shown in Table II. The values of the diattenuation are nearly the same for each region within the sample, which indicates that the direction of the c-axis with respect to the sample normal is nearly the same for the area sampled. However, the direction of the principal axis can change depending upon the region. Although the measured principal axis angles γ are referenced to the laboratory reference frame, the relative direction of the principal axes are not dependent upon sample placement. The differences between the values of γ for the 3 subregions in Figure 5 is small, but well outside the error limits of the measurement. This shows that the 2-MGEM is very sensitive to small changes in crystallite orientation if the diattenuation is reasonably large. Furthermore, rotations of the crystallite about the c-axis would marginally change the measured diattenuation but not change the direction of the principal axis. This observed variation of the principal axis is due to small variations in the direction of the c-axis; showing that natural aragonite has many small-angle grain boundaries.

If the sample is cut such that the c-axis is perpendicular to the sample surface, then the diattenuation is small but measurable. Figure 6 shows a region that contains several subregions where the c-axis is nearly perpendicular to the sample surface and one subregion where the c-axis is considerably off-normal. The values of the diattenuation and direction of the principal axis for the three lettered subregions are

given in Table III. Using Equation 5, the direction of the c-axis for subregion a is 67.1 ± 1°. This region has also been measured using EBSD, where the c-axis angle is 68.9 ± 3°. The error limits include both stochastic errors and systematic error associated with the placement of the sample in the experiments. As can be seen, the 2-MGEM and EBSD measurements agree.

Table III. The values of the diattenuation N and the direction of the principal axis γ for the 3 subregions of Figure 6.

	N	γ (°)
A	0.1629±0.0015	57.2±0.2
B	0.0062±0.0013	-48±4
C	0.0032±0.0013	54±16

The subregions b and c of Figure 6 correspond to crystallites where the c-axis is nearly perpendicular to the sample surface. The small value of the diattenuation can come from two different sources. First, the c-axis can be slightly tilted off-normal, and the projection of the c-axis onto the sample surface will contribute to the diattenuation. Secondly, the small refractive index difference between the a and b directions will also generate a contribution to the diattenuation. If the c-axis were directly perpendicular to the sample surface, the diattenuation of subregion b would result in a refractive index difference of 0.0053 between the a and b directions; this is consistent with the measured values of the refractive indices. Some EBSD comparison measurements were also taken on different regions of the aragonite c-perp sample and are discussed in Appendix 6.2.

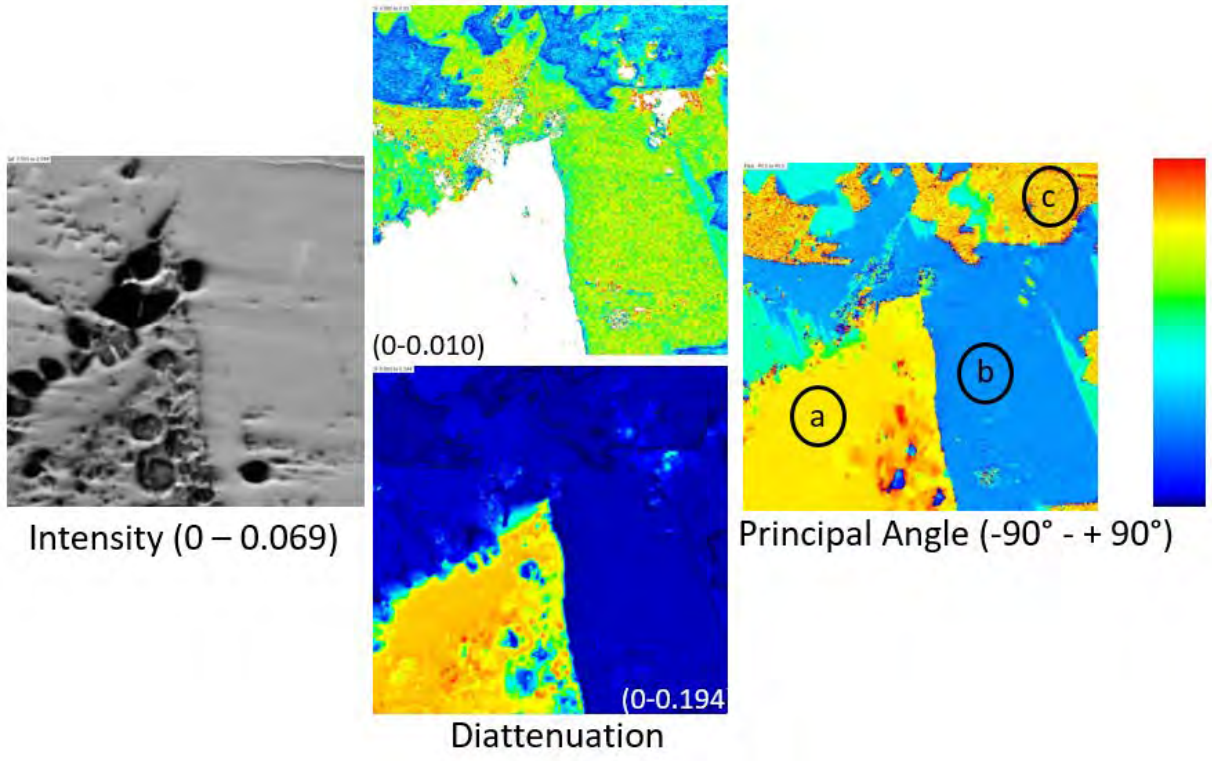

Figure 6. 2-MGEM data from sample c-perp region 5. The color scale is to the right and the values in parentheses give the ranges. The scale is 1.535 X 1.47 mm. Note that the diattenuation data is presented twice using different scales.

3.3 Granite

Granite is a common rock found in the earth's crust and consists mostly of quartz and feldspar. Because granite is so common in the earth's crust, it is often found as a primary aggregate constituent in concrete. The main atomic building block of granite is a distorted SiO_4 unit. Undistorted, this unit is

isotropic and will not produce optical birefringence. However, virtually all SiO_4 units in any silicate compound found in the earth's crust are distorted and are coupled with many other atoms, such as Al, K, Na, Ca, Fe, etc. As a result, most crystallites found in granite have low symmetry (monoclinic or triclinic) but with small birefringence. Even with small birefringence, many crystallites of granite do show a diattenuation N and therefore a direction of principal axis γ. These crystallites can be identified from 2-MGEM data.

Figure 7 shows the image, diattenuation, and direction of the principal axis for two regions of a granite sample. The averaged values of the diattenuation and direction of the principal axis are shown in Table IV. Region 4 is shown in the top panel of Figure 7. The intensity image shows some cracks but does not show strong indications of crystallite boundaries. However, it is clear that images of the diattenuation and direction of the principal axis do distinguish between different crystallites and, in some cases, show that cracks are just cracks in the same crystallite. Subregions R4a and R4c are clearly distinguishable from the diattenuation and principal axis maps but are not distinguishable at all from the intensity plot. Subregion R4c shows a very small diattenuation, and as a result, cannot measure the direction of the principal axis accurately at all. The large crack at the bottom of the intensity map in the top panel of Figure 7 is not between different crystallites but rather a crack in the same crystallite R4d. This can be seen by comparing the values of the diattenuation and direction of the principal axes of subregions R4b and R4d, which are the same within error.

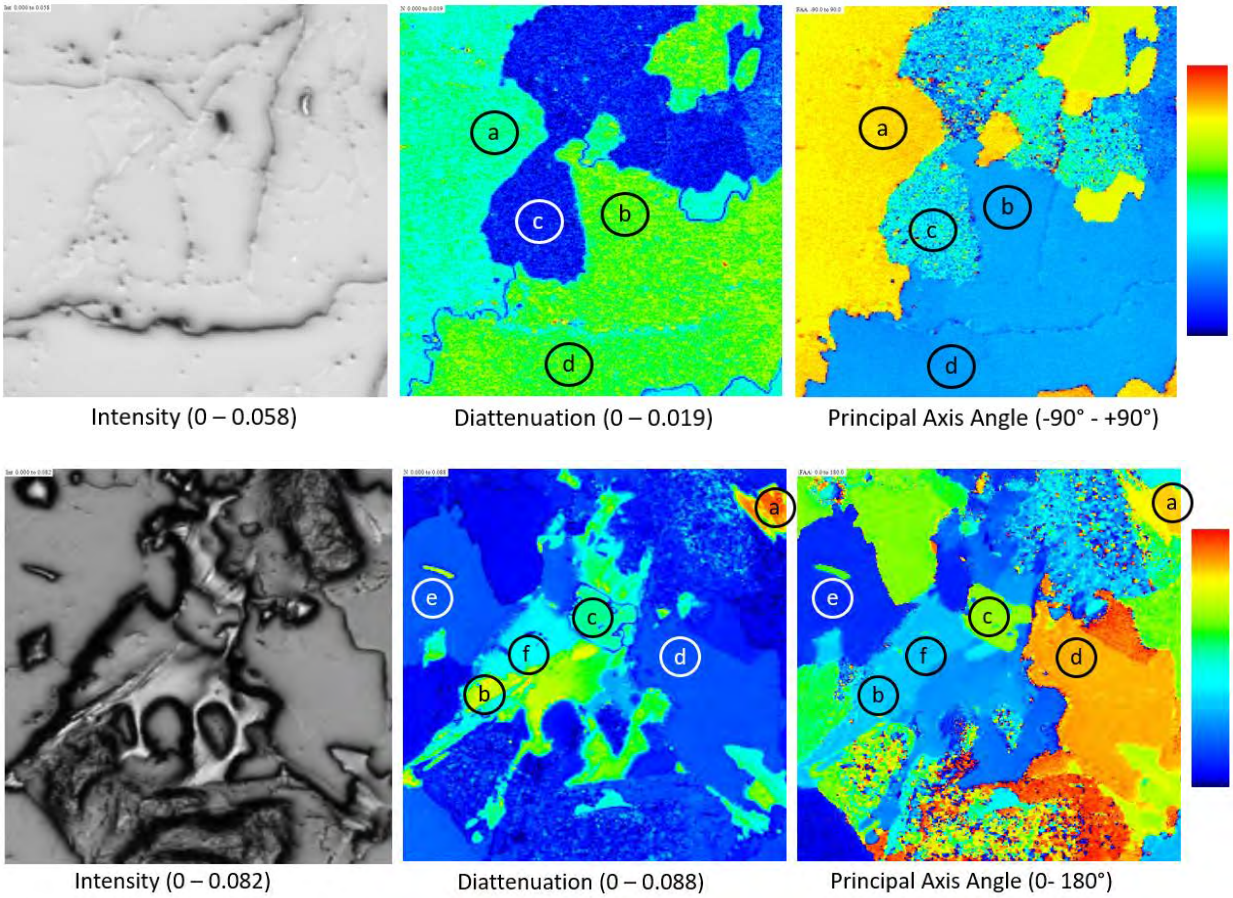

Figure 7. 2MGEM data for granite. The top panel shows region 4 with dimensions 1.105 XZ 1.130 mm, and the bottom panel shows region 5 with dimensions 1.57 X 1.60 mm.

Region 5, shown as the bottom panel of Figure 7, shows a region of the granite sample where there is a distinguishable feature from the intensity map. The bright feature near the center of the intensity map also has a diattenuation that is considerably larger than the diattenuations of the surrounding area. Subregions R5b, R5c, and R5f all have large diattenuations, but subregion R5c has a considerably different principal axis angle than does R5b and R5f. Subregion R5a has an even higher diattenuation resulting in a very accurate measurement of the direction of the principal axis. Moreover, using equations 6, $|\Delta n| \geq 0.05$, which is very large for a silicate-based feldspar. Subregions R5d and R5e have nearly the same diattenuation, but quite different principal axis angles.

Table IV. 2-MGEM data averages for the selected subregions indicated in Figure 7. Subregion R4 corresponds to the top images of Figure 7 and subregion R5 corresponds to the bottom images of Figure 7. The maximum and minimum of the color scale is given below each image.

Subregion	R4 N	R4 γ (°)	R5 N	R5 γ (°)
a	0.0091±0.0010	54.7±2.9	0.0783±0.0039	-29.0±0.5
b	0.0113±0.0009	-41.6±2.8	0.0607±0.0041	57.9±1.5
c	0.0012±0.0008	-40±30	0.0486±0.0045	-60.9±10.6
d	0.0110±0.0009	-43.1±2.8	0.0134±0.0011	-26.4±2.1
e	----	----	0.0113±0.0009	18.6±2.3
f	----	----	0.0327±0.0023	57.1±1.4

3.4 Feldspars

3.4.1 Microcline and Orthoclase

Microcline and orthoclase are both feldspars with the chemical formula $KAlSi_3O_8$. Microcline is triclinic and its polymorph orthoclase is monoclinic. Microcline is marginally more stable than orthoclase, but often the two polymorphs are found together as evidenced by the cross-hatch twinning often found in microcline/orthoclase rocks. Both are commonly found in granite, so they both are common components in the aggregates found in concrete.

Optically, both minerals are biaxial and require 3 refractive indices to describe the interaction of visible light with the material at a single wavelength. Since these minerals have lower symmetry then orthorhombic, the principal optical axes will be dependent on the wavelength of light, but this change will be very small for visible light. Previously measured refractive indices typically lie in the range of ~1.51 – 1.54 with a birefringence of <0.007. The small birefringence means that any measured diattenuation from the material will be small.

A single crystal of orthoclase was examined both using spectroscopic ellipsometry and with the 2-MGEM. The spectroscopic ellipsometry showed that the refractive index at 577 nm was 1.520 to 1.524 (±0.002 for the three principal axes), with a maximum birefringence of 0.002 – 0.006). 2-MGEM measurements on pristine surfaces showed that the diattenuation was 0.0065 ± 0.0008. The calculated birefringence from Equations 6 is ~0.004, which is in agreement with the measured birefringence from the spectroscopic ellipsometry measurements. Furthermore, the spectroscopic ellipsometry measurements showed that this orthoclase crystal has a bandgap of ~3.5-3.8 eV.

A microcline/orthoclase rock was cut to expose 4 different faces and each face was optically polished so that 2-MGEM measurements could be taken. The 2-MGEM data is shown in Figures 8 and 9. The intensity shown in Figure 8 shows no indication of grain boundaries, but the diattenuation and direction of the principal axis does show the presence of grains in this region. This is emphasized from the optical pole figure, also shown in Figure 8. The pole figure was calculated assuming that $N_{max} = 0.015$, which is

somewhat high for microcline/orthoclase, which may indicate that the high diattenuation regions are not these materials but rather an impurity.

Figure 9 shows similar data from the 2-MGEM measurements of a different face of the cut microcline/orthoclase rock near an obvious crack in the sample. Just above and below the crack, the diattenuation is ~0.0055±0.0026, but shows obvious striations; the average value of the principal angle is ~2°±16°. Since the diattenuation is so small, accurate measurement of the principal axis is not possible. These striations in the diattenuation may indicate the presence of microcline/orthoclase twinning in the rock. There are two other smaller but noticeable regions at the top of the image which are only slightly noticeable from the intensity image but quite obvious from the diattenuation and principal axis images. The diattenuation of both features is nearly the same (0.0126 ± 0.0018), but the direction of the principal axis is quite different (-34° and +36° ±3° for the left and right features, respectively). The high value of the diattenuation possibly indicates that these features are from impurities in the rock rather than from microcline/orthoclase.

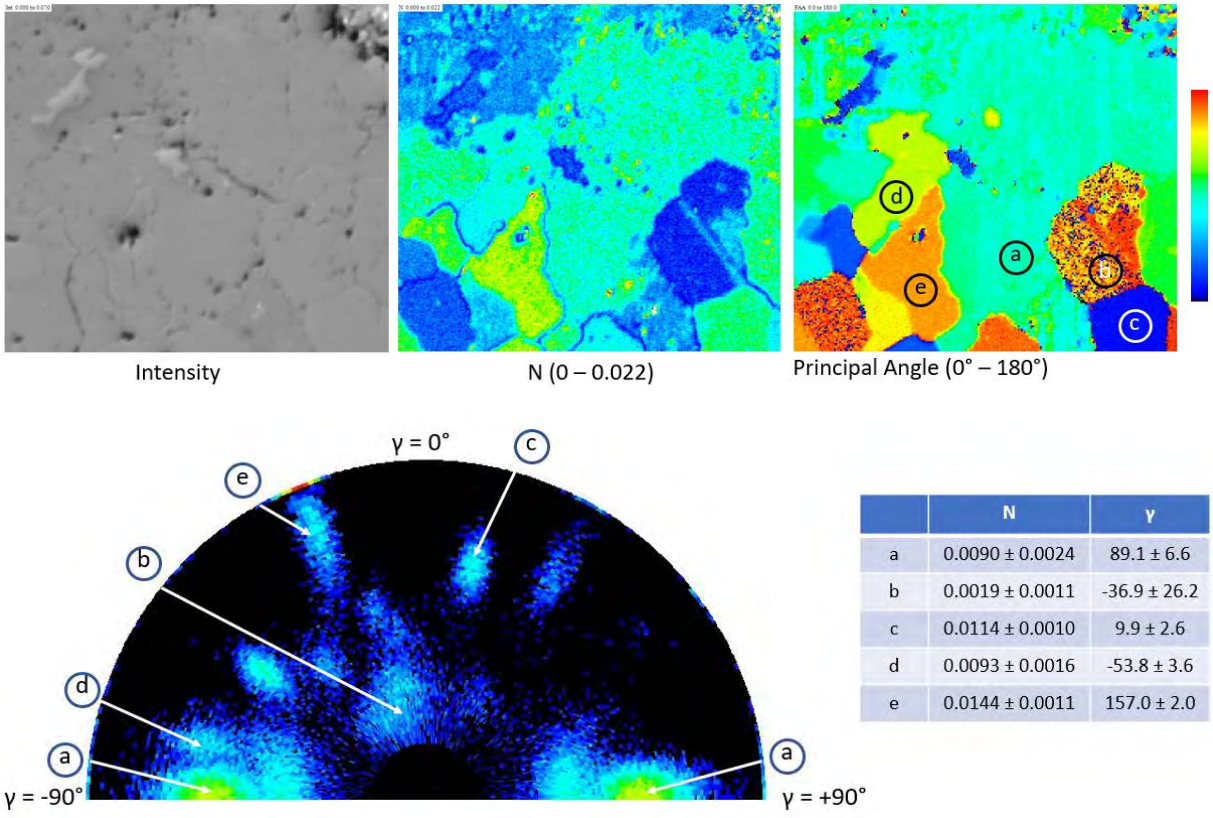

	N	γ
a	0.0090 ± 0.0024	89.1 ± 6.6
b	0.0019 ± 0.0011	-36.9 ± 26.2
c	0.0114 ± 0.0010	9.9 ± 2.6
d	0.0093 ± 0.0016	-53.8 ± 3.6
e	0.0144 ± 0.0011	157.0 ± 2.0

Figure 8. Microcline B region 5, showing the intensity image, diattenuation N and Principal Axis angle γ (top). The associated optical pole figure and the values of 5 subregions (bottom).

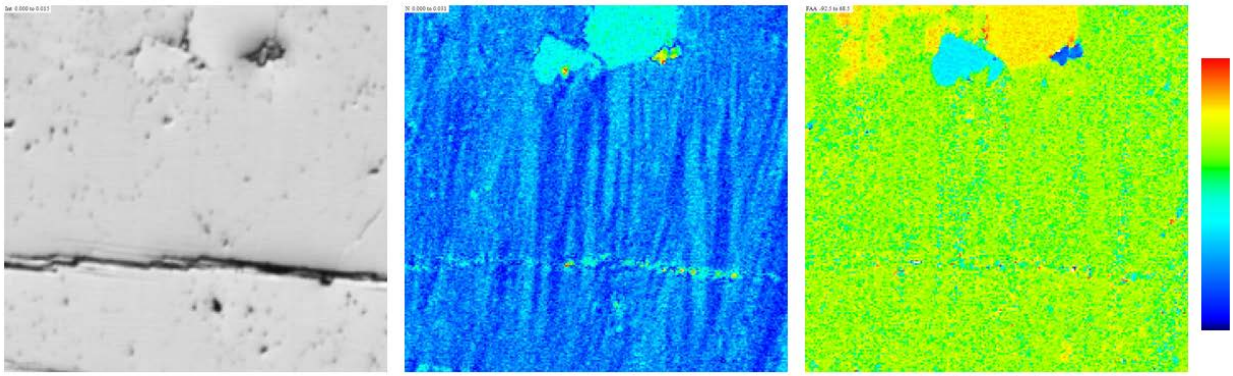

Figure 9. 2-MGEM measurements from microcline/orthoclase region D6 showing the intensity image, diattenuation N and Principal angle.

3.4.2 Labradorite

Labradorite is a feldspar mineral with chemical composition $(Ca,Na)(AlSi)_4O_8$ where the fraction Ca/(Ca+Na) = 50-70%. Its crystal point group is 1 bar, which means that it is triclinic with inversion symmetry. The known refractive indices range from 1.55 to 1.57 with a birefringence of ~0.010 at 589 nm making the material marginally birefringent. Using Equations 6, the predicted maximum diattenuation would be ~0.014. Labradorite crystals have the peculiar characteristic that they often display the incandescent optical effect known as Labradorescence. That is, light reflection from a labradorite crystal will often have a green-gold color hue to it, which cannot be attributed to impurities. This effect is caused from light reflection from submicroscopic planes oriented in a single direction with lamella separation of 100-300 nm.

Figure 10 shows the 2-MGEM data from a region of the cut and polished labradorite sample. Most of the sample shows uniform diattenuation and direction of the principal axis. However, both N and γ show a thin line, marked as b in Figure 10, where N is significantly larger than in region a, and γ is quite different. This sample also shows a streak across the sample (regions c, d, and e) where the N is quite large. These regions are obviously impurities that are incorporated into the labradorite crystal.

Figure 11 shows the 2-MGEM data from another section of the labradorite sample that was cut ~90° from the sample shown in Figure 10. Here there is no predominant region where N and γ are the same, but rather several different regions, all with small values of N, but quite different values of γ. It can be seen that regions a, d, and e all have very small values of N, and therefore very inaccurate measures of γ.

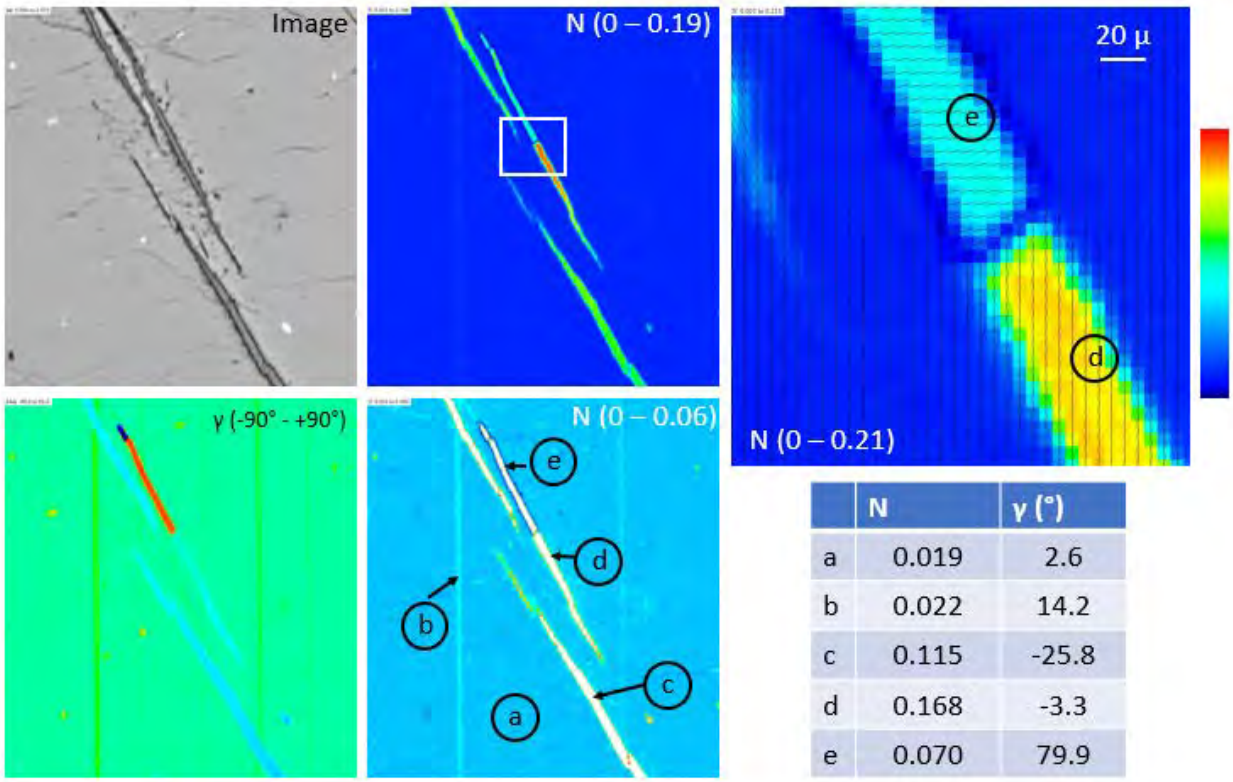

	N	γ (°)
a	0.019	2.6
b	0.022	14.2
c	0.115	-25.8
d	0.168	-3.3
e	0.070	79.9

Figure 10. Labradorite region A3. 1.78 X 1.92 mm. The diattenuation N image to the right shows a high resolution image of the boxed region where each pixel represents a 5 X 5 micron area. The lines in each pixel indicate the direction of the principal axis. The values of the diattenuation N and principal axis γ for the 5 lettered regions are shown in the table to the lower right.

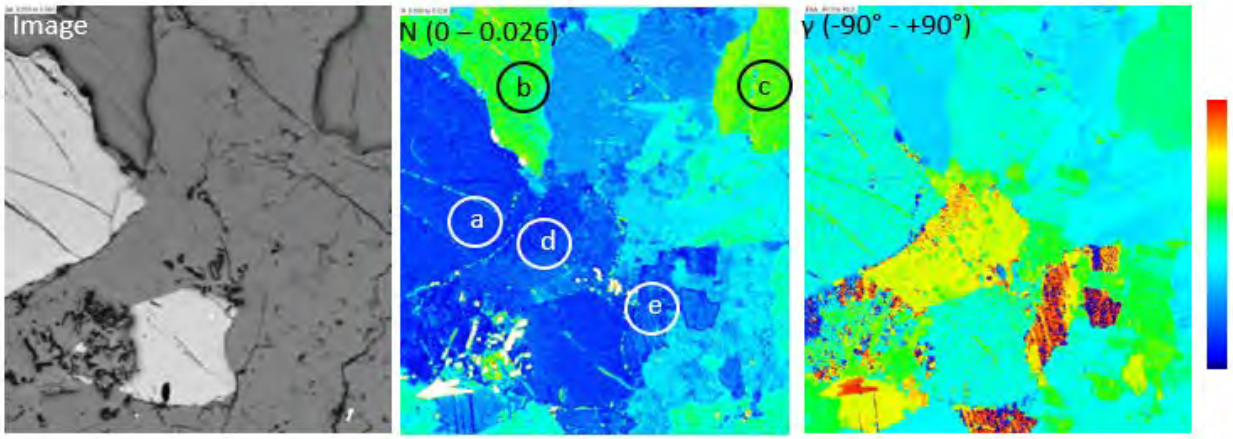

	N	γ (°)
a	0.003	-16±21
b	0.015	152±4
c	0.016	5±4
d	0.003	33±24
e	0.004	62±19

Figure 11. Labradorite A1. 1.70 X 1.86 mm, where the sample face was cut ~90° to that of the sample of Figure 10.

3.5 Concrete

Concrete is a complex building material that contains small rocks (called aggregates) bonded together with a cement paste. The aggregates are critical to the strength of concrete but can be any type of rock, all of which may contribute to or degrade from the strength of the concrete. This is particularly true when the concrete is exposed to environmental effects, including normal weathering, stresses from use or many other effects.

Figure 12 shows 2-MGEM measurements of a cut and polished concrete sample measuring 4 X 4 mm. The optical image corresponds to a high f# microscope (f# ~ 12). Therefore, light reflecting off the rough cement paste will be reflected out of the collection cone of the instrument and will not contribute to the measurement. In fact, any light that does come from these regions is significantly depolarized and therefore give no useful information.

Regions 1 and 2 shown in Figure 12 do give good measurements of the diattenuation and principal axis angle with small depolarization. However, these regions show a very low diattenuation and scrambled values of the principal axis; this is contrasted to region 3, a and b, which show very large diattenuation and an easily measured direction of the principal axis angle. Since the maximum diattenuation is ~0.23, one can surmise that these aggregates are carbonate-based rocks (limestone or marble), while regions 1 and 2 are silicate-based rocks.

Regions a and b of Figure 12 are expanded and shown in Figure 13. The diattenuation is represented by the color code using the scale to the right of Figure 12 where $N_{max} = 0.23$ and the principal axis direction is indicated by the line drawn in each pixel. The pixel size is 5 X 5 microns, so grain boundary definition cannot be determined to closer that ~5 microns; this is clearly seen in Figure 13.

Region 3 of Figure 12 shows a particularly interesting color pattern in that it does not appear to have sharp boundaries. An optical pole figure of this region is shown in Figure 14, that shows the variation of the direction of the c-axis of a calcite/dolomite crystallite. This may be an indication of stress within the crystallite, variation of composition of the crystallite, etc.

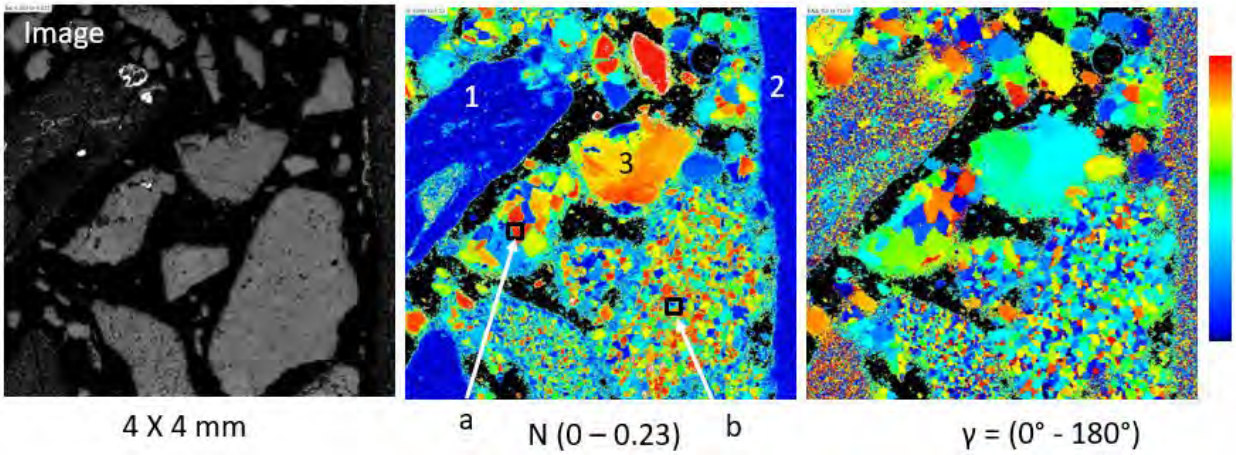

Figure 12. Concrete sample examined using 2-MGEM. The sample size is 4 X 4 mm with pixel size 5 X 5 micron. (801 X 801 = 641,601 pixels). The lettered regions a and b are also shown on an expanded scale in Figure 13, and the numbered regions 1, 2, and 3 are discussed in the text.

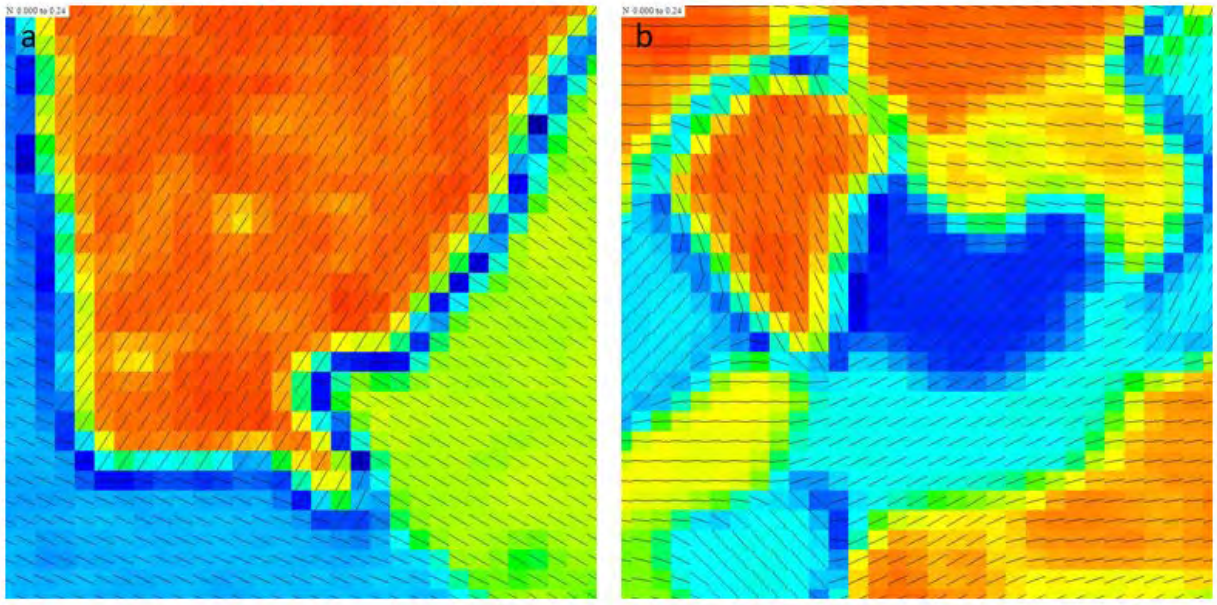

Figure 13. Expanded regions a and b from Figure 12 showing the color-coded diattenuation and the direction of the principal axes as the line in each pixel. The maximum diattenuation N_{max} = 0.23 and the color scale to the right in Figure 12 is used.

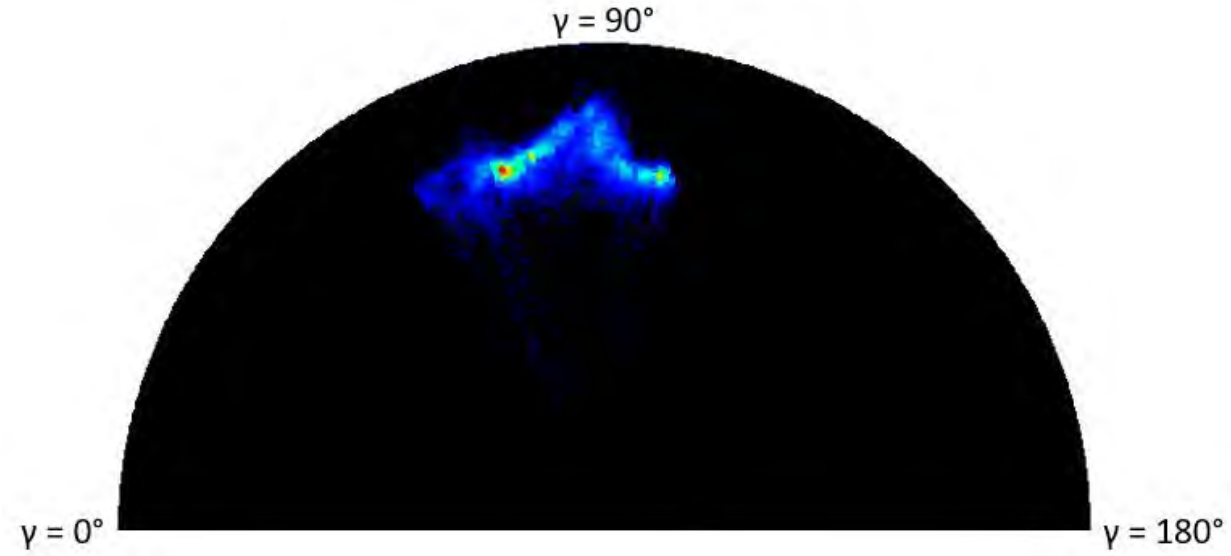

Figure 14. Optical pole figure for region 3 of Figure 12. See the discussion of Figure 3 for a description of the optical pole figure.

4. CONCLUSIONS

4.1 Comparison of 2-MGEM and EBSD (Jellison et. al 2018)

Clearly, 2-MGEM and EBSD give similar results on the examined samples of calcite, dolomite and aragonite. There are, however, several differences: some major, some minor.

1. Sample preparation: With 2-MGEM measurements, light is reflected from large changes in refractive index, and the collection cone for the reflected light is quite small. Consequently, roughly polished samples will reflect most of the light out of the system, which will not change the results of the ellipsometry parameters but will reduce the signal to noise ratio. Therefore, better results from 2-MGEM measurements are obtained with optically polished surfaces. On the other hand, EBSD is sensitive to the top 5 nm of the sample. Any damage in this layer (such as residual strain from coarse polishing that was not removed by fine polishing) will adversely affect EBSD measurements, requiring a much better polish than would be required for 2-MGEM measurements. In addition, EBSD measurements of insulating samples (such as calcite, dolomite and aragonite) require a conductive coating such as evaporated carbon be applied to the sample surface to prevent charging; this coating will also degrade the EBSD pattern quality slightly. A conductive coating would also adversely affect 2-MGEM measurements. Conversely, sample preparation is easier for 2-MGEM measurements.
2. Resolution: The optical resolution of the present 2-MGEM system is ~6 μ but has been demonstrated at ~4 μ using different optics (Jellison and Hunn, 2008). Further improvement to < 1 μ is possible. The resolution of EBSD is primarily limited by the electron interaction volume, which is sample and beam energy dependent. This is typically 10-250 nm, which is considerably better than can be obtained using any visible light instrument.
3. Parameters measured and accuracy on good regions: The 2-MGEM measures 8 parameters at each pixel with an accuracy of 0.001-0.002 out of ±1. These parameters are then used to determine the diattenuation N and direction of the principal axis γ, which then can be used to determine the optic axis orientation of the pixel. For a uniaxial crystallite, these measurements can be interpreted in terms of the direction of the optic axis, where γ is determined modulo 180°. For a well-formed crystallite, the accuracy in the direction of the fast axis γ is 0.1° - 0.2°, while the accuracy of the optic axis off-normal θ is 1° - 8°, depending on the magnitude and error of the diattenuation N. On the other hand, a good EBSD measurement of a uniaxial crystallite will determine the orientation of all axes with a stochastic error of 0.3° to 2.0°. However, the systematic errors resulting from the accuracy of the placement of the sample into either instrument, thereby reducing the absolute accuracy significantly of both techniques. Because of distortions, this can be a significant problem for EBSD.
4. Time of Measurement: Each measurement of a 2-MGEM pixel will take ~ 20-25 milliseconds, which includes waveform acquisition and Fourier analysis to determine the 8 parameters. Often several measurements are taken at each pixel so that a standard deviation can also be calculated, making the total measurement time 100-150 milliseconds per pixel. The time of data acquisition for EBSD is highly sample-dependent in that the computer time required to analyze the Kikuchi patterns will depend on the crystal structure (although the computer analysis is generally much shorter than the CCED integration time to capture each individual EBSD pattern). Typically, measurement times for these samples were ~20 milliseconds per pixel, which is comparable with faster 2-MGEM measurements.
5. Image distortion: 2-MGEM measurements are obtained by scanning the sample under the optical beam, which is nearly perpendicular to the surface. EBSD measurements are obtained with both the electron beam and the recording phosphor and detector off-normal. As the sample is scanned,

pincushion distortion results; this can be corrected to first order, but still leaves second order distortions. This is particularly important when the scanning area is large, as evidenced in Figure 4. This EBSD image distortion can in principle be corrected by performing smaller beam-scanned maps, with stage motion used to bring different regions of the sample directly under the beam, followed by software stitching of the individual, smaller maps into a montage. (However, the JSM-6500F instrument used here is not capable of such automated stage-scan experiments.)

6. Regions where good measurements cannot be made: Not all regions of a polycrystalline sample can be measured by either technique. For 2-MGEM measurements, the measurable region is roughly the size of optical resolution, ~6 μ for this 2-MGEM. If there are multiple crystallites in such a region, each of the 8 parameters would be averages of these parameters over all the crystallites in the region, resulting in some depolarization and unreliable measurements. With an EBSD measurement, multiple crystallites in a pixel would result in an incorrect determination of the crystallite orientation. However, a more serious problem with good EBSD measurements occurs in regions where the top ~5 nm of the sample are disordered from polishing or carbon deposits.
7. 2-MGEM measurements require birefringent crystallites and the higher the birefringence, the better the measurements. EBSD can be performed on crystallites of any symmetry. This may not be a significant disadvantage for 2-MGEM, since most crystallites in rocks are birefringent.
8. 2-MGEM measurements can be performed in air, EBSD measurements require a vacuum.

4.2 General Conclusion

The 2-MGEM measures the diattenuation N very accurately to ±0.001 where N varies from -1 to 1. The 2-MGEM measurement also determines the direction of the principal axis angle γ , but the accuracy of the γ measurement depends on the magnitude of N. For example, if N~0.2, then the accuracy of the γ measurement is typically ±0.2° - 0.3°; If N~0.05, then the accuracy of γ becomes ~1°. In many cases, this accuracy is sufficient to determine the crystallite boundaries in a sample.

If the sample consists of uniaxial materials with a large birefringence (such as calcite or dolomite), it is possible to measure the direction of the optic axis of the crystallite with high accuracy. This data can then be plotted as an optical pole figure of the sample measured. This pole figure is similar to that which would be produced from x-ray of EBSD measurements but differs in three respects. First, the measurement of γ is modulo 180°, so the optical pole figure would not distinguish between an optical axis orientation of (θ, ϕ) and (θ, ϕ+180°). Secondly, the accuracy of the θ measurement is quite inaccurate when the optic axis is perpendicular to the sample surface or when it is in the surface plane of the sample. Thirdly, the optical pole figure is not able to detect crystallite rotations about the optic axis.

If the sample is orthorhombic (where there are 3 refractive indices for light polarized along the 3 principal, orthogonal axes of the crystallite), less information is obtained. Such a crystal is aragonite, where one of the refractive indices is considerably smaller than the other two. This large difference in refractive indices allows for the determination of the c-axis if the c-axis is significantly different from the surface normal. If the c-axis is nearly parallel to the surface normal, then the diattenuation is a function of the small difference in the refractive indices n_a and n_b, as well as the small tilt of the c-axis off the surface normal. However, the (N, γ) data can be used to limit the possible orientations of the crystallite.

If the sample is monoclinic or triclinic, then there are 4 or 6 refractive indices that describe the light refractive power of the material, and the directions of the principal axes depend on the wavelength of light. Many of the crystallites found in granite and other geological silicate materials examined in this report fall into this category. The essential issue is that the 2-MGEM measures two parameters (N and γ) very accurately, but orthorhombic, monoclinic and triclinic crystallites would require 3 or more measurements to determine the orientation of the crystallites IF the refractive indices were known. Other

techniques, such as micro x-ray fluorescence can aid in the determination of the atoms comprising a crystallite, but give no indication as to the orientation of the crystallites. Micro Raman could also be used, but again the information is incomplete. In short, a complete identification of a crystallite including chemical composition, polymorph, and crystallite identification is a very complicated task, and many appropriate techniques should be brought to bear to address the identification.

This work shows that the 2-MGEM is potentially an important additional characterization tool to be used by geologists and others interested in the microstructure of rocks. While it is very difficult to extract exact crystallographic orientation from the (N, γ) data from orthorhombic and lower symmetry materials, , this data on a pixel-by-pixel level is a very good indication of crystallite boundaries. For geologists, this is extremely important information and cannot be determined easily using any other technique.

One of the primary disadvantages of our present 2-MGEM system is the optical resolution, presently restricted to ~6 microns. An effort is presently underway to improve this resolution to better than 1 micron.

5. FUTURE WORK

This report shows that the 2-MGEM adds considerably to the knowledge of crystallite identification and orientation in rocks and therefore in aggregates in concrete. Comparisons with EBSD show that both techniques have advantages and disadvantages, and on regions where good measurements have been obtained, the results agree. Other techniques with micron-level detection resolution, such as micro x-ray fluorescence (mXRF) and high-resolution Raman could also be applied to these samples, but we have yet to do this on many samples (See Appendix 6.3 for one set of experiments).

The most interesting results from the 2-MGEM measurements have been made on carbonate materials, where an optical pole figure of each crystallite can be obtained. However, the carbonate rocks are not as susceptible to neutron damage as silicate materials. Therefore, we propose to explore in detail several granite samples using all the mentioned techniques (2-MGEM, EBSD, mXRF, Raman) on the same areas of a granite sample.

Some 2-MGEM measurements of granite have already been done (see Section 3.3 and Figure 7), which show that 2-MGEM can identify crystallites in the material. Granite is a very complicated combination of SiO_2 – based materials, all of which are birefringent and therefore can be detected using the 2-MGEM. However, we do need to also do mXRF, EBSD, and micro Raman measurements to better classify the crystallites. All of the pure polymorphs of SiO2 (quartz, tridymite, stishovite, etc.) are birefringent, but the birefringence is relatively small. This translates to a small but measurable diattenuation.

One of the other issues concerns the crystal structure near the grain boundaries, which should be detectable using the 2-MGEM. However, this will require an improvement of the spatial resolution of the 2-MGEM. The present resolution is ~6 microns, but this can be improved to ~1 micron with an optimized optical design.

6. APPENDIX

6.1 EBSD comparison with 2-MGEM for dolomite (Jellison et. al 2018)

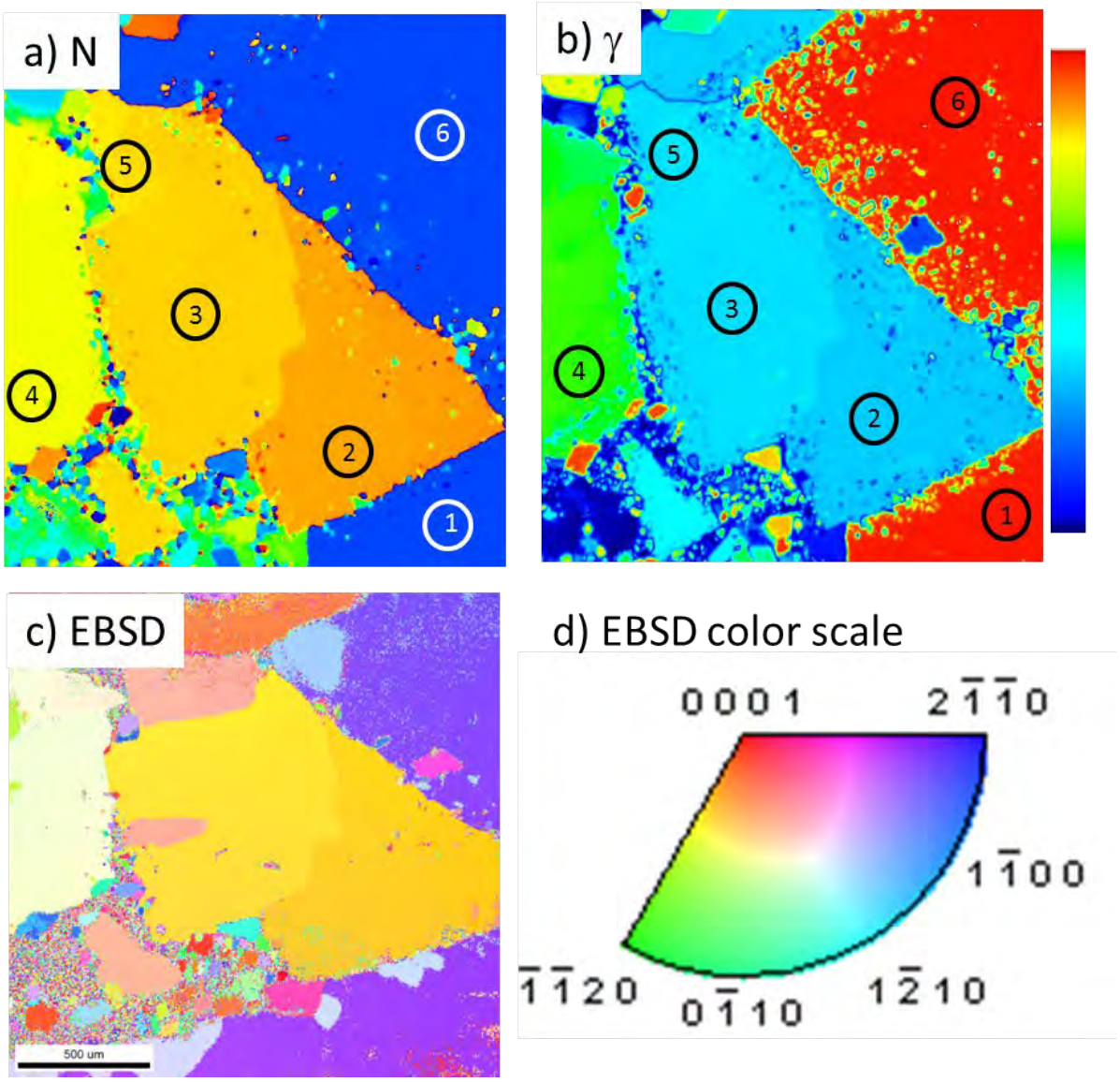

Figure A-1. Comparison of 2-MGEM data with EBSD data for the dolomite sample discussed above and displayed in Fig. 2. a) 2-MGEM diattenuation; b) 2-MGEM fast axis angle; c) EBSD data presented as the inverse pole figure with the 0001 direction projected out of the page, d) scale map used for the EBSD data. All data was taken on a 5 x 5 μ grid. The region numbers are circled 1-6 and discussed after Table A1.

The comparison between EBSD and 2-MGEM for the region of the dolomite of Figure 2 is shown in Figure A-1, where the 2-MGEM diattenuation N and direction of the fast axis γ are shown in comparison with the EBSD inverse pole figure map of nearly the same region of the dolomite sample.

It is clear from this direct comparison that both EBSD and 2-MGEM show many of the same features of the crystallites, but the EBSD data is distorted along both the horizontal and vertical directions. This is known as the pincushion distortion, and is a result of non-linearity in the SEM scan coils, and is pronounced when a high-resolution-optimized SEM is used to perform very low magnification scans, as is the case here. This effect is exacerbated by the 70° tilt necessary for SEM EBSD measurements. Since the light beam used in a 2-MGEM experiment is nearly perpendicular to the sample surface and the sample is scanned in the plane of the sample surface, this distortion is absent in 2-MGEM measurements.

To compare the angles of the optic axis determined from EBSD and 2-MGEM measurements, additional EBSD measurements were taken on the dolomite sample in each region shown in Fig. 11 where the measurement area was restricted to 45 X 45 μ with a 1 μ step. This restriction in measured area essentially eliminates the pincushion distortion, allowing for a better comparison of the angles determined using the two techniques. The EBSD measurements are interpreted in terms of the orientation of the crystal unit cell using the Bunge convention of Euler angles. The 2-MGEM measurements are interpreted in terms of the direction of the optic axis, where the angle θ is restricted to 0° to 90° and the FAA is determined modulo 180° and can be reported as -90° to 90° or as 0° to 180°.

The directions of the optic axis from EBSD data are determined from the Bunge Euler angles ϕ_1 and Φ. The third EBSD measured angle ϕ_2 is ignored since it represents a rotation about the optic axis and cannot be seen optically from a uniaxial crystal. The angle θ for the EBSD measurement is determined from Φ: ; if $\Phi < 90°$, then $\theta = \Phi$, else $\theta = 180° - \Phi$. The EBSD determination of γ is made from ϕ_1, where the following conversions are made:

1. Dolomite is a negatively birefringent crystal, so the γ is perpendicular to the optic axis.
2. Since the Bunge definition of a positive rotation of ϕ_1 is counterclockwise and the 2-MGEM convention of the optic axis is clockwise, $\gamma(\text{EBSD}) = -\phi_1$
3. Due to the trigonal symmetry of dolomite, EBSD measurements of ϕ_1 are modulo 120°.
4. The 2-MGEM measurements of γ are modulo 180°.

Table A-I shows the resulting optic axis angles from the EBSD and 2-MGEM measurements. The standard deviations between the two measurements are 2.5° for θ and 1.5° for FAA. As noted above, the error of θ as determined using 2-MGEM measurements is quite large when θ is near 0° or 90°. In addition, some of the differences between the two techniques may be due to the initial orientation of the crystals in the respective systems.

Table A-I Comparison of the angles of the optic axis determined using EBSD and the 2-MGEM. The EBSD Euler angles ϕ_1, Φ, and ϕ_2 are determined using the Bunge convention, and the EBSD and optics angles θ and γ described in the text.

	EBSD					2-MGEM Optics		EBSD – 2-MGEM Optics	
Region	ϕ_1	Φ	ϕ_2	θ	γ	θ	γ	θ	γ
1	61.6°	97.0°	266.4°	83.0°	-61.6°	82.0°	-63.7°	1.0°	2.1°
2	293.6°	31.3°	1.1°	31.3°	66.4°	35.1°	66.2°	-3.8°	0.2°
3	299.6°	34.4°	355.7°	34.4°	60.4°	36.7°	60.6°	-2.3°	0.2°
4	128.8°	131.1°	75.1°	48.6°	51.2°	51.1°	50.4°	-1.8°	0.8°
5	119.1°	144.3°	67.3°	35.7°	60.9°	36.9°	58.5°	-1.2°	2.4°
6	61.9°	94.5°	268.1°	85.5°	-61.9°	82.0°	-63.7°	3.5°	1.8°

6.2 EBSD comparison with 2-MGEM for c-perp aragonite (Jellison et. al 2019)

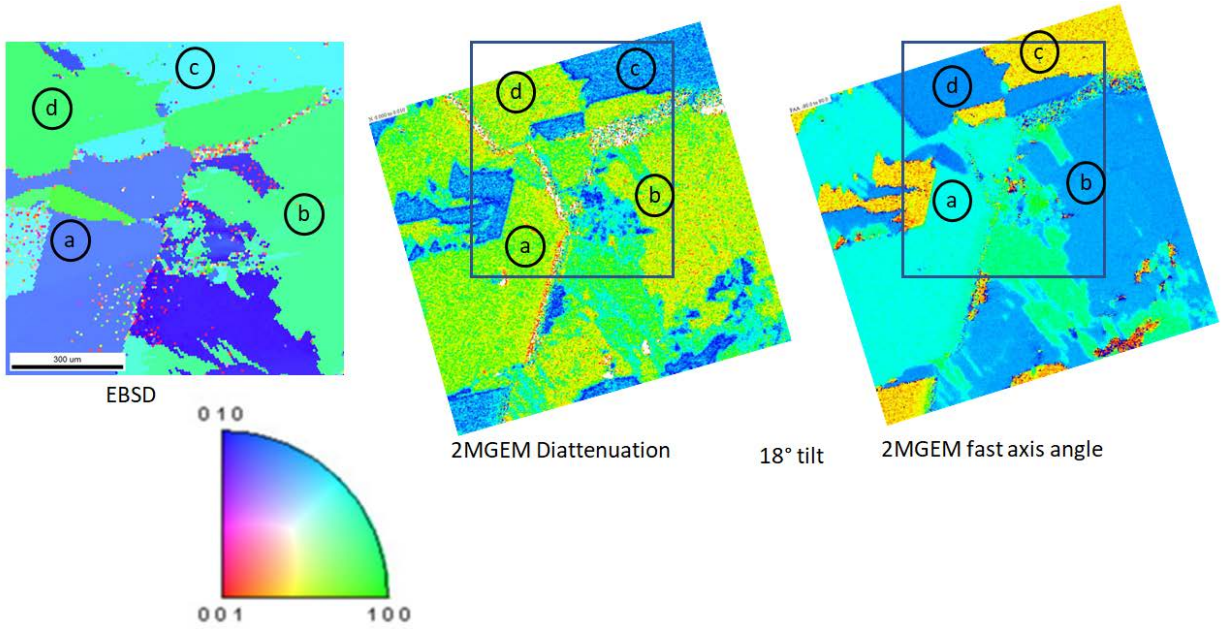

Figure A-2. Comparison of 2MGEM data from region 2 and EBSD data from nearly the same region. Note that the EBSD data shows some significant pincushion distortion for such a large scan. Moreover, there is a significant registration issue in that the EBSD sample was rotated ~18° with respect to the 2MGEM data. The color code beneath the EBSD plot shows the orientation of each pixel.

Figure A-2 shows a comparison between EBSD and 2-MGEM for the cperp aragonite sample. While the EBSD image shows significant pincushion distortion and the registration is rotated ~18° with respect to the 2-MGEM data image, both techniques provide images of the crystallites as well as their boundaries. In the EBSD image, there are several off-color dots that are the result of the inability of the software to determine the crystallographic orientation from the Kirkuchi patterns. The color patterns in the EBSD image shows that all the observed crystallites are oriented with their c-axes nearly-normal to the sample surface; this agrees with the small diattenuation observed from the 2MGEM images of the data.

Detailed comparisons of the 2-MGEM and EBSD techniques were performed on subregions b of Figure A-2 and subregion a of Figure 6. If the calculated values of N and γ fall within the error-bounded experimental values, then that value of (θ, ϕ, ψ) is considered a valid value and plotted as black in Figure A-3; if the calculated values of N and γ do not fall within the error-bounded experimental values, then that area is plotted as white. Thus, the black areas of Figure A-3 represent the acceptable values of the Euler angles describing the crystallite orientation for a given value of N and γ, including errors. For comparison purposes, the Euler angles from the EBSD measurement are plotted as a gray ellipse, where the extent of the ellipse indicates the estimated error (both stochastic and systematic) of the EBSD measurement. While the relative errors of the EBSD and 2-MGEM instruments can be very good, both instruments are susceptible to the systematic error resulting from sample placement; it is estimated that the combined systematic error is ~3°.

Region b of Figure A-2 has a very small diattenuation, indicating that the c-axis is nearly perpendicular to the sample surface. However, the refractive index difference in the a and b directions can also contribute to the diattenuation. As a result, the 2-MGEM data can only say that the θ angle of the

crystallite is small, and that there is some correlation between the ϕ and ψ angles. Region a of Figure 6 is different, in that the 2MGEM data specifies the θ and ϕ angles but cannot determine the ψ angle. This is very similar to the results for uniaxial calcite and dolomite analyzed by Jellison et. al (2018), where the ψ angle is degenerate. In both regions, the EBSD data agrees with an acceptable orientation of the crystallite direction from the 2-MGEM data.

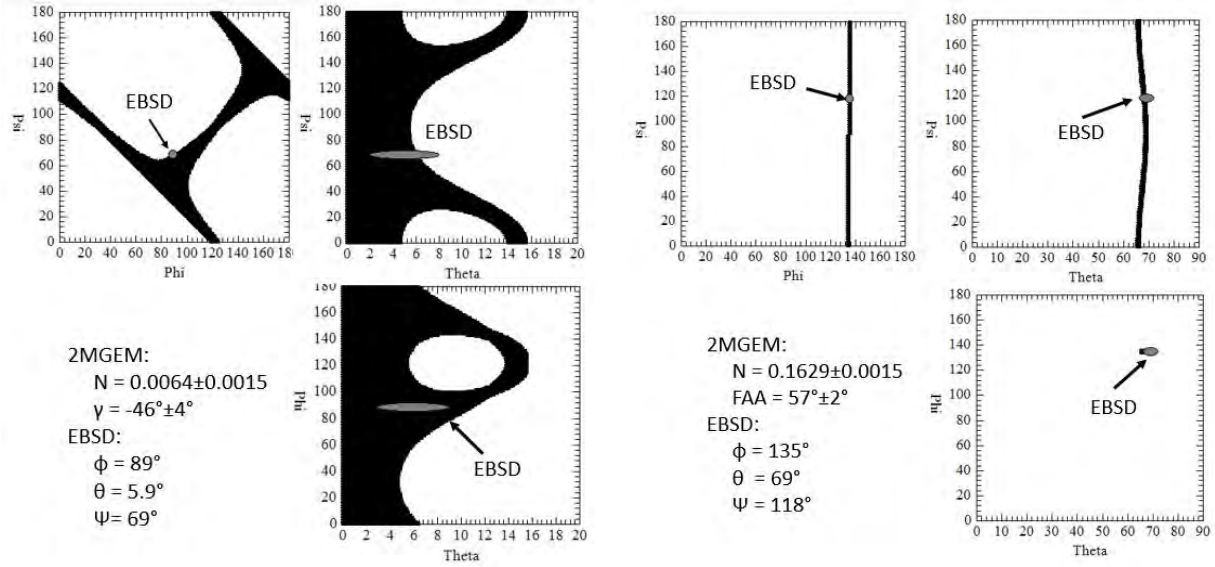

Figure A-3. The possible Euler angles (Phi = ϕ, Psi = ψ,Theta = θ) for the orientation of the crystallites of subregions R2b (left) and R5a (right). See the text for a description of the calculation technique. The gray ellipse indicates the measured Euler angles from EBSD, where the extent of the ellipse indicates the estimated error, both stochastic and systematic.

6.3 Comparison of x-ray fluorescence (mXRF) and 2-MGEM of concrete aggregates

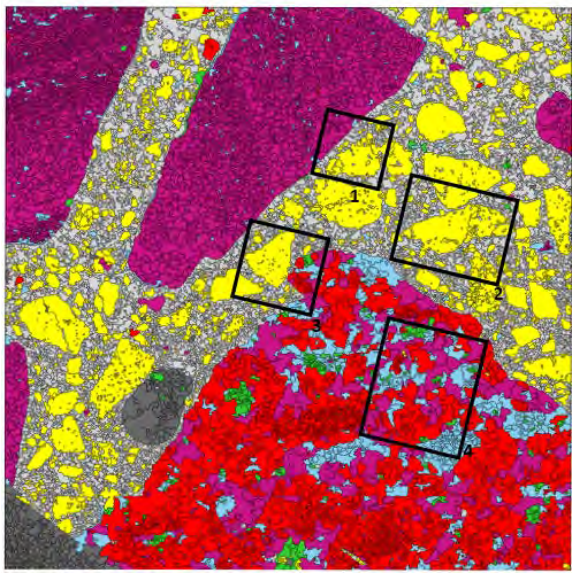

Figure A-4. Micro X-ray fluorescence (mXRF) image of aggregates in concrete. The black boxes indicate regions also measured using 2-MGEM. Yellow: $CaCO_3$ (calcite/aragonite); red: quartz, etc. (SiO_2); medium violet-red: $KalSi_3O_8$ (microcline/orthoclase feldspar); sky-blue: $KAl_3Si_3O_{10}$ (Muscovite?); gray: cement. Scale: 12 x 12 mm

Figure A-4 shows an image obtained from x-ray fluorescence measurements of concrete aggregates, as well as the black boxes where 2-MGEM measurements are made. As can be seen, many of the smaller aggregates are carbonate materials and the larger particles are silicate-based materials. The carbonate materials are quite uniform in color, but the silicate-base materials are significantly more complicated.

Figure A-5 top shows the 2-MGEM data from region 1 of Figure A-4. The intensity image shows that the central particle is well-defined but contains several cracks. The depolarization factor β shows that there is very little depolarization over the central particle or in the wedge particle partially captured in the upper left of the image. The diattenuation N and direction of the principal axis γ of the central particle show definite crystallites, and the magnitude of the diattenuation shows that the particle is carbonate-based, which agrees with the mXRF image. The (N,γ) data can be converted to an optical pole figure, as is shown in Figure A-5.

Far less can be discerned from the wedge in the upper left of Figure A-5 top, identified as microcline/orthoclase feldspar from mXRF. Microcline/orthoclase rocks are known to be very complicated minerals, often with both phases present. Since they do have quite similar optical properties, it is quite reasonable that the 2-MGEM data, with an optical resolution of ~6 microns, would not be able to discern very small crystallites and the 2-MGEM data images would represent only an average.

This difficulty is also shown in Figure A-5 bottom, which shows 2-MGEM data from region 4. From the mXRF data, this particle is extremely complicated, consisting of micro crystallites of quartz, feldspar and muscovite and possibly variants with similar compositions. The 2-MGEM image shows that this sample was quite rough and a better polish might be needed to get better data. However, the 2-MGEM image of the diattenuation N does show several distinctive regions. At the bottom of the N image, there is a particle that is red/yellow, (N~0.04), which transitions to green (N~0.03) above it, indicating a grain boundary; this transition cannot be seen from the intensity image or the mXRF data.

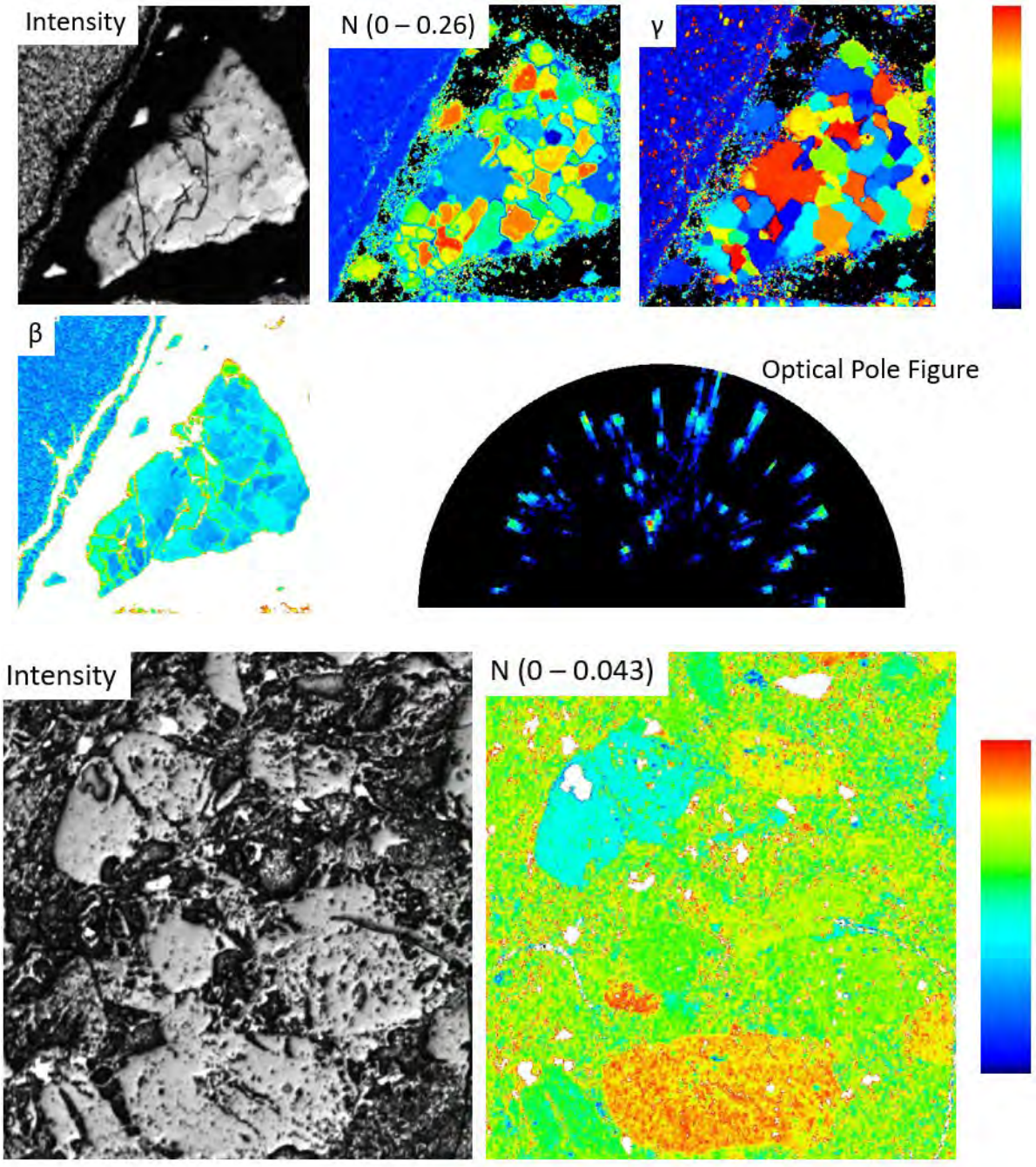

Figure A-5. 2-MGEM images of region 1 (top) and region 4 (bottom) of the concrete aggregates shown in Figure A-4.

7. REFERENCES

Berek, M., "Universaldrehtischmethoden," Berlin (1924).

Bragg, W. L., "The refractive indices of calcite and aragonite," *Proceedings of the Royal Society of London, Series A*, **105**, 370-386 (1924).

Davis, B. L., and L. H. Adams, "Kinetics of the calcite ⇌ aragonite transformation" *Journal of Geophysical Research,* **70,** 433-441 (1965).

Fazio, E., Punturo, R., Cirrincione, R., Kern, H., Pezzino, A., Wenk, H-R., Goswanmi, S. and Mamtani, M. A., "Quartz preferred orientation in naturally deformed mylonitic rocks (Montalto shear zone-Italy): a comparison of results of different techniques, their advantages and limitations," Int. J. Earth Sci. **106**, 2259-2278 (2017).

Giorla, A., "Development of non-linear Fast Fourier Transform (FFT) solvers for the simulation of irradiation-induced expansion in concrete," ORNL/SPR-2018/793 (2018)

Graves, H., Le Pape, Y., Naus, D., Rashid, J., Saouma, V., Sheikh, A. and Wall, J., "Expanded Material Degradation Assessment (EMDA), Volume 4: Aging of Concrete," NUREG/CR-7153, ORNL/TM-2011/545, US Nuclear Regulatory Commission (2014).

Huang, W.-L., "Synthetic polycrystalline aragonite to calcite transformation kinetics: experiments at pressures close to the equilibrium boundary,": *Mineralogy and Petrology*, **79**, 243-258, (2003).

Japan Nuclear Energy Safety Organization, "Review Manual for Aging Management Technical Evaluation,' Tokyo: JNES-RE-2013-9012 92013).

Jellison, Jr., G. E. and Modine, F. A., "Two-Modulator Generalized Ellipsometry: Experiment and Calibration," Appl. Opt. **36**, 8184-8189 (1997); "Two-Modulator Generalized Ellipsometry: Theory," Appl. Opt. **36**, 8190-8198 (1997).

Jellison, Jr., G. E., Hunn, J. D. and Rouleau, C. M., "Normal-incidence generalized ellipsometry using the two-modulator generalized ellipsometry microscope (2-MGEM)," Appl. Opt.**45**, 5479-5488 (2006).

Jellison, Jr., G. E., and Hunn, J. D., "Optical anisotropy measurements of TRISO nuclear fuel particle cross-sections: the method," J. Nuclear Materials **372** 36-44 (2008).

Jellison, Jr., G. E., Leonard, D. N., Anovitz, L., Parish, C. M., Specht, E. D., and Rosseel, T. M., "Crystallographic Orientation of uniaxial calcite and dolomite determined using reflection generalized ellipsometry," *J. Appl. Phys.* **124** 223102 (2018).

Jellison, Jr., G. E., Leonard, D. N., Cheshire, M., Anovitz, L., Specht, E. D., and Rosseel, T. M., "Crystallographic Orientation of orthorhombic aragonite using reflection generalized ellipsometry," Manuscript submitted for publication. (2019).

Le Pape, Y., Tajuelo Rodriguez, E., Arregui-Mena, J'D., Giorla, A., Anovitz, L., and Rosseel, T. M., "Validation of Combining Imaging Techniques-Based Characterization of Concrete Mineral Constituents for the Development of the MOSAIC Tool," ORNL/SPR-2019/1098 (2019a).

Le Pape, Y., Tajuelo Rodriguez, E., Arregui-Mena, J'D., Giorla, A., Anovitz, L., and Rosseel, T. M., Neutron-irradiation-induced damage assessment in concrete using combined phase characterization and nonlinear and nonlinear FFT simulation, Proceedings of the 10th International Conference on Fracture Mechanics of Concrete and Concrete Structures (2019b) .

Newnham, R. E., "Properties of materials: anisotropy|symmetry|structure", Oxford University Press Inc., New York (2005).

Rosseel, T. M., Gussev, M. N., Mora, L. F., "The Effects of Neutron Irradiation on the Mechanical Properties of Mineral Analogues of Concrete Aggregates," *Proceedings of the 18th International Conference on Environmental Degradation of Materials in Nuclear Power Systems – Water Reactors*, *Vol..2* , J. H. Jackson et al., The Minerals, Metals & Materials Series, pp. 151-161 https://doi.org/10.1007/978-3-319-68454-3_14 (October 2017)

Silva, C., Rosseel, T. M., & Kirkegaard, M. C., "*Radiation-Induced Changes in Quartz, A Mineral Analog of Nuclear Power Plant Concrete Aggregates," **Inorg. Chem., 2018,** DOI:* 10.1021/acs.inorgchem.8b00096

Panozzo-Heilbronner, R. and Pauli, C., "Integrated spatial and orientation analysis of quartz c-axes by computer-aided microscopy," J. Struct. Geol. **15**, 369-383 (1993).

Prior, D. J., Boyle, A. P., Brenker, F., Cheadle, M. C., Day, A., Lopez, G., Peruzzo, L., Potts, G. J., Reddy, S., Spiess, R., Timms, N. E., Trimby, P., Wheeler, J. And Zetterstrom, L., "The application of electron backscatter diffraction and orientation contrast imaging in the SEM to textural problems in rocks," Am. Min. **84**, 1741-1759 (1999).

Prior, D. J., Mariani, E. and Wheeler J., Ch. 26 in "Electron backscatter diffraction in Materials Science," Schwartz, A. J. et. al.,(Eds.) Springer Science + Business Media, LLC (2009).

Rosseel, T. M., Maruyama, I., Le Pape, Y., Kontani, O., Gioria, A. B., Remec, I., Wall, J. J., Sircar, M., Andrande, C. and Ordonez, M., "Review of the Current State of Knowledge on the Effects of Radiation on Concrete," J. Adv. Concr. Technol. **14**, 368–383 (2016).

8. PUBLICATIONS

Jellison, Jr., G. E., Leonard, D. N., Anovitz, L., Parish, C. M., Specht, E. D., and Rosseel, T. M., "Crystallographic Orientation of uniaxial calcite and dolomite determined using reflection generalized ellipsometry," *J. Appl. Phys.* **124** 223102 (2018).

Jellison, Jr., G. E., Leonard, D. N., Cheshire, M., Anovitz, L., Specht, E. D., and Rosseel, T. M., "Crystallographic Orientation of orthorhombic aragonite using reflection generalized ellipsometry," Manuscript accepted for publication in the Journal of Applied Physics. (2019).

Jellison, Jr., G. E., Leonard, D. N., Anovitz, L. M., and Rosseel, T. M., "Normal Incidence Generalized Ellipsometry Examination of Geological Materials," Presented at the 8th International Conference on Spectroscopic Ellipsometry (ICSE8), Barcelona, Spain, May 26-31, 2019.